

POLITECNICO DI TORINO

Master of Science in Aerospace Engineering

Master Thesis

**Modelling and Analysis of the
Decay Phase for Space Objects in
LEO**



Supervisor:
prof. Nicole Viola
Co-Advisor:
prof. Edmondo Minisci

Candidate:
Francesco Vincelli

Academic year 2019/2020

Abstract

This Thesis presents a low-fidelity approach to model and analyze the decay phase for space objects (space debris) originally orbiting in Low Earth Orbits (LEO). This approach is used to better characterize some of the involved uncertainties, which are propagated through the propagation of the orbit in order to characterize the re-entry time. In particular, the main source of uncertainty lies in the prediction of solar and geomagnetic indices which is performed through time series analysis techniques. The indices influence the Total Mass Density (TMD) in the Thermosphere, i.e. the layer of the Earth atmosphere from about 90 [km] of altitude to between 500 and 1000 [km]. During the decay phase, a low-fidelity 3 degree of freedom (DoF) propagator is used and the only perturbation force considered is the aerodynamic drag, which is the main one in LEO. Alongside the propagator, the Thermosphere model NRLMSISE00 is adopted in order to calculate TMD with some uncertainty depending on the indices values, which defines the re-entry time window when the propagation stops at the altitude of end orbit. Validation of the model is presented using the well-known test case of GOCE re-entry, while a demonstration of the potential of the model is given through the analysis of classes of high area to mass ratio space objects.

Acknowledgments

Here we are, at the end of my academic path. It has been hard, but fulfilling. First of all, I have to say thank you to my mom Marisa and my dad Giuseppe, who always supported me and helped me to succeed. My mom has been like a friend for me, I always could talk with her about everything and this is precious for me. My dad always provided for me and made me smile when I was angry or sad. The other members of my family (aunts, uncles and grandparents, without exception) played also an important role in this challenge. When I was down, my family pulled me up, pushing me to go further and for this reason I couldn't do anything without them. Moreover, a special thank you goes to my friends. They gave me precious moments of freedom for my mind, smiling and having fun together. This helped me to regain energy every time. They are my second family. Last but not least, my girlfriend Claudia. We are together from almost the beginning of our journey at Politecnico. We've been having beautiful moments and also hard time, which we overcame together, but we got memories which we'll keep forever. I loved my University years with her and I'd do all over again (yeah, even the exams).

In the end, I want to say a huge "Thank you!" to prof. Edmondo Minisci (as he prefers, "Ed"), my supervisor at Strathclyde, and prof. Nicole Viola, who put me in touch with him. Ed made me feel welcome immediately, and I appreciated all the time he spent with me and all his tips. My period abroad has been really a nice experience, and one of the reasons lies in the relationship I had with him and his research group "ICE Lab".

Thank you.

Table of contents

Abstract	I
Acknowledgments	II
1 Introduction	1
1.1 Literature review	2
1.2 Aerodynamic drag	6
1.3 Thermospheric indices and models	8
1.4 Brief overview of orbit propagators	12
2 Modelling Phase	14
2.1 Thermosphere Model	14
2.2 Prediction of the indices	15
2.2.1 Prediction of daily $F_{10.7}$	17
2.2.2 Prediction of daily 3-hour a_p	20
2.3 Calculation of re-entry time window	29
2.3.1 Identifying maximum and minimum TMD	29
2.3.2 Orbit Propagator	32
3 Validation Phase	40
3.1 GOCE re-entry modelling	40
3.1.1 Prediction of solar and geomagnetic indices for GOCE	42
3.2 GOCE simulations	46
4 Analysis of a practical application	50
4.1 High area to mass ratio space objects	51
4.2 Simulations and results	52
4.2.1 Low solar activity and low uncertainty results	55
4.2.2 Medium solar activity results	59
4.2.3 High solar activity results	61
5 Conclusions	64

List of tables

2.1	Operations to obtain the catalog of the future $F_{10.7}$ indices	20
2.2	Operations to obtain the catalog of the future a_p indices	24
2.3	Inputs for the testing of the linearity/non-linearity of the Thermo- sphere model NRLMSISE00	30
2.4	Computational times for the minimum re-entry time of a $10 \frac{m^2}{kg}$ space debris on 01/05/2018	32
3.1	GOCE Data Set used in the simulations for the validation of the model	42
3.2	The re-entry time window for GOCE	47
4.1	Planned simulations for high area to mass ratio space debris	52
4.2	Initial orbital conditions corresponding to TLE of ISS orbit on 11/02/2020 at 00:00 UTC used in the simulations	54
4.3	Results in days for low solar activity and low uncertainty simulations	55
4.4	Relative errors for low solar activity and low uncertainty simulations	56
4.5	Results in days for medium solar activity and medium uncertainty simulations	59
4.6	Relative errors for medium solar activity and medium uncertainty simulations	59
4.7	Results in days for high solar activity and high uncertainty simula- tions	61
4.8	Relative errors for high solar activity and high uncertainty simulations	62
5.1	Results of the simulations for $10 \frac{m^2}{kg}$ space object during low solar activities with artificial reduction of the uncertainty	65

List of figures

1.1	Schematic map of current literature	5
2.1	First test: fitting solar indices from 2005 to the 30/04/2018 and forecasting values until the end of 2021	17
2.2	Fitting solar indices from 2000 to the end of 2016 and forecasting values until the end of 2019	21
2.3	Fitting solar indices from 1965 to the end of 1999 and forecasting values until the end of 2009	21
2.4	Comparison among different confidence intervals(the top left is set to 80%, the top right is set to 90% and the one below is set to 95%)	22
2.5	Fitting solar indices from 1980 to 30/04/2018 and forecasting values until the end of 2025	23
2.6	Best result: fitting solar indices from 1980 to 30/04/2018 and forecasting values until the end of 2021	23
2.7	Fitting geomagnetic index a_{p0-3} from 2005 to 30/04/2018 and forecasting values until the end of 2021 with default settings of <i>Prophet</i>	24
2.8	Fitting a_{p0-3} from 2005 to 30/04/2018 and forecasting values until the end of 2021 with logistic growth (limited between 0 and 40)	25
2.9	Fitting geomagnetic index a_{p0-3} from 2005 to 30/04/2018 and forecasting values until the end of 2021	25
2.10	Fitting geomagnetic index a_{p3-6} from 2005 to 30/04/2018 and forecasting values until the end of 2021	26
2.11	Fitting geomagnetic index a_{p6-9} from 2005 to 30/04/2018 and forecasting values until the end of 2021	26
2.12	Fitting geomagnetic index a_{p9-12} from 2005 to 30/04/2018 and forecasting values until the end of 2021	27
2.13	Fitting geomagnetic index a_{p12-15} from 2005 to 30/04/2018 and forecasting values until the end of 2021	27
2.14	Fitting geomagnetic index a_{p15-18} from 2005 to 30/04/2018 and forecasting values until the end of 2021	28
2.15	Fitting geomagnetic index a_{p18-21} from 2005 to 30/04/2018 and forecasting values until the end of 2021	28

2.16	Fitting geomagnetic index a_{p21-24} from 2005 to 30/04/2018 and forecasting values until the end of 2021	29
2.17	Testing linearity of NRLMSISE00 on 01/05/2018 at 416000 [m] of altitude	31
2.18	Testing linearity of NRLMSISE00 on 01/01/2020 at 302000 [m] of altitude	31
2.19	Orbital plane reference frame	34
2.20	ECI reference frame	35
2.21	Celestial Equatorial coordinates	38
3.1	http://www.esa.int/ESA_Multimedia/Images/2009/05/GOCE_in_orbit	41
3.2	Prediction of $F_{10.7}$ solar index for 2013 and 2014 (above) and corresponding particular of the predicted values (below)	43
3.3	Prediction of a_{p0-3} (left) and a_{p3-6} (right) geomagnetic index for 2013 and 2014	44
3.4	Prediction of a_{p6-9} (left) and a_{p9-12} (right) geomagnetic index for 2013 and 2014	44
3.5	Prediction of a_{p12-15} (left) and a_{p15-18} (right) geomagnetic index for 2013 and 2014	45
3.6	Prediction of a_{p18-21} (left) and a_{p21-24} (right) geomagnetic index for 2013 and 2014	45
3.7	Comparison between predicted (left) and real (right) values of $F_{10.7}$ in 2013 and 2014	45
3.8	Details from figures 3.7 of the considered years, with on the left the predicted values and on the right the real ones	46
3.9	Altitude range comparison for the re-entry time window of GOCE	48
3.10	GOCE's orbit decay	48
3.11	Top view of GOCE's orbit decay	49
4.1	Prediction of solar index $F_{10.7}$ adopted in the simulations	53
4.2	Altitude evolution during the decay phase for space object of $10 \left[\frac{m^2}{kg} \right]$ in low solar activity minimum re-entry time simulation	57
4.3	Altitude evolution during the decay phase for space object of $1 \left[\frac{m^2}{kg} \right]$ in low solar activity minimum re-entry time simulation	57
4.4	Orbit decay phase for space object of $10 \left[\frac{m^2}{kg} \right]$ in low solar activity minimum re-entry time simulation	58
4.5	Orbit decay phase for space object of $1 \left[\frac{m^2}{kg} \right]$ in low solar activity minimum re-entry time simulation	58
4.6	Altitude evolution during the decay phase for space object of $10 \left[\frac{m^2}{kg} \right]$ in medium solar activity minimum re-entry time simulation	60
4.7	Altitude evolution during the decay phase for space object of $1 \left[\frac{m^2}{kg} \right]$ in medium solar activity minimum re-entry time simulation	60

4.8	Altitude evolution during the decay phase for space object of 10 $[\frac{m^2}{kg}]$ in high solar activity minimum re-entry time simulation	62
4.9	Altitude evolution during the decay phase for space object of 1 $[\frac{m^2}{kg}]$ in high solar activity minimum re-entry time simulation	63
5.1	Re-entry time windows comparison for every set of simulations per- formed	65

Chapter 1

Introduction

Since humankind first started to launch objects in order to put them in orbit around the Earth re-entry predictions have always been a challenging field due to the troubles to know deterministic values of the variables of interest. Several studies have been conducted trying to deepen the knowledge about this argument and a lot of models and methods have been carried out (section 1.1). The main reason is that on average, two small tracked debris re-enter the Earth's atmosphere every day, one medium object re-enter once a week and large object re-enter in a year [14]. The latter could survive the impact with the atmosphere and pose a risk to the population and the infrastructure. Moreover, space traffic will increase in the near future and these averages could increase, too. For this reason, recent guidelines of Inter-Agency Space Debris Coordinator Committee (IADC) adopted by ESA and the other agencies require that re-entry of satellites occurs within 25 years of the end-of-life [11], hence re-entry will be increasingly relevant.

However, "re-entry predictions" is a general term and there are many aspects related to it. The Decay Phase for space objects in Low Earth Orbit (LEO) is one of them. Essentially, this is the phase until the object reaches about 120 km of altitude where the free fall flight ends and usually break up can occur. One of the variables of interest in this kind of problems is the re-entry time, that is the time the object takes to reach the altitude of break up from its initial conditions. As it will be introduced in the following sections this variable can be achieved only with some degree of uncertainty, therefore it is more accurate talking about re-entry time windows.

This work is structured as follows. In the next sections of this chapter it will be provided an overview of the current literature, models and main steps that are currently involved in this kind of studies. Then, in chapter 2, it will be explained how the results presented in this work have been achieved and the choices which have been made through the modelling phase. Once the model was created, a validation of the model itself has been necessary to be sure that the future results can be promising. A suitable well-known case has been identified in the Gravity Field and Steady-State Ocean Circulation Explorer (GOCE) spacecraft re-entry due to the vast amount of data available as it will be presented in chapter 3. In order to give an overview of the capabilities of the model on practical cases, a set of simulations was performed on classes of high Area to Mass ratio debris in predicted periods with different solar and geomagnetic activities. The results are summarised in chapter 4. As it will be explained, these simulations have been selected for reasons related to the computational costs and to enrich the studies which have been carried out in [11], where the solar and geomagnetic indices were constants, giving a re-entry time windows due to the uncertainty related to the prediction of the indices. Conclusions and discussions will be at the end of the thesis in chapter 5.

1.1 Literature review

First of all, an overview among different papers and articles published by agencies, universities and the rest of the scientific community has been necessary in order to have a clear view of the state of art about re-entry phase studies. A schematic map of the main research groups reported in the literature is illustrated in Fig.1.1, where it is possible to identify three main groups of research (Geul's [1] and Horsley's [3] papers in the purple box can't be allocated exactly in one of the others groups because their topics are more general):

- the green one is about a group of researchers from the European Space Agency (ESA);
- the blue one consists of the members of the Aerospace Department in University of Strathclyde (Glasgow, UK);
- the orange one has not a defined location but it is composed of worldwide

researchers dealing with the Thermosphere models and their effects on the re-entry phase;

It is important to specify that these are not the only groups who are currently working in this field but the ones that have been taken into account in this summary literature review.

Concerning the Virgili's group in ESA, the main topics are:

- The illustration of the tools used by ESA during re-entry [13] [14];
- The orbit determination from different sources of data (such as radar-based and GPS based) [7] [14];
- The presentation of real re-entry cases as the GOCE and the VEGA-01 AVUM campaigns [12] [13];

On the other hand, the future steps that they suggest following are:

- Provide dedicated sensors able to collect data for re-entering objects and share the acquired data to automate the re-entry process prediction and increase accuracy.
- Further reduce the uncertainty about the state of the atmosphere during re-entry and use different atmosphere models and solar activity inputs for the next re-entry campaigns;
- Investigate how to extend data from the real cases analysed to other bodies;

With regards to the Aerospace group at University of Strathclyde, the major focus on re-entry is about uncertainties. In particular, it is possible to find in the literature:

- A classification of different kind of uncertainties and methods to propagate them (DSMC, linear and non-linear surrogates) [8] [10];
- A comparison among vary non-intrusive non-linear surrogates and a description of 3-DoF and 6-DoF analysis [8];
- An introduction to machine learning approach [8];
- An application of these methods and analysis to space objects with high area to mass ratio [11];

Besides, ideas for following works are suggested:

- Further improve machine learning in this field;
- Use a more complex model for uncertainty acting on atmosphere parameters;
- Include uncertainties treatment in the 6-DoF dynamics investigating the scalability of the uncertainty on the re-entry time concerning A/m parameter;

The last major group is composed of six different research groups who published papers providing an overview of the Thermosphere models and the uncertainties in their parameters. Essentially, it is reported:

- A classification of solar, geomagnetic and solar wind indices [2];
- A comparison of thermospheric density models already implemented (JACCHIA, MSIS, DTM, etc) and illustration about their chronological evolution [2] [5] [6] ;
- A presentation of possible current time atmospheric density correction to increase accuracy [15];
- An illustration of the structure of the Thermosphere [4];
- A description of solar event phenomena and their effect on re-entry prediction [9];

Moreover, some improvements are still requested in this field:

- Further investigations about the impact of the thermospheric density modeling on orbital mechanics are needed;
- More accurate thermospheric models should be developed;
- Real-time corrections of atmospheric density should be implemented when possible;

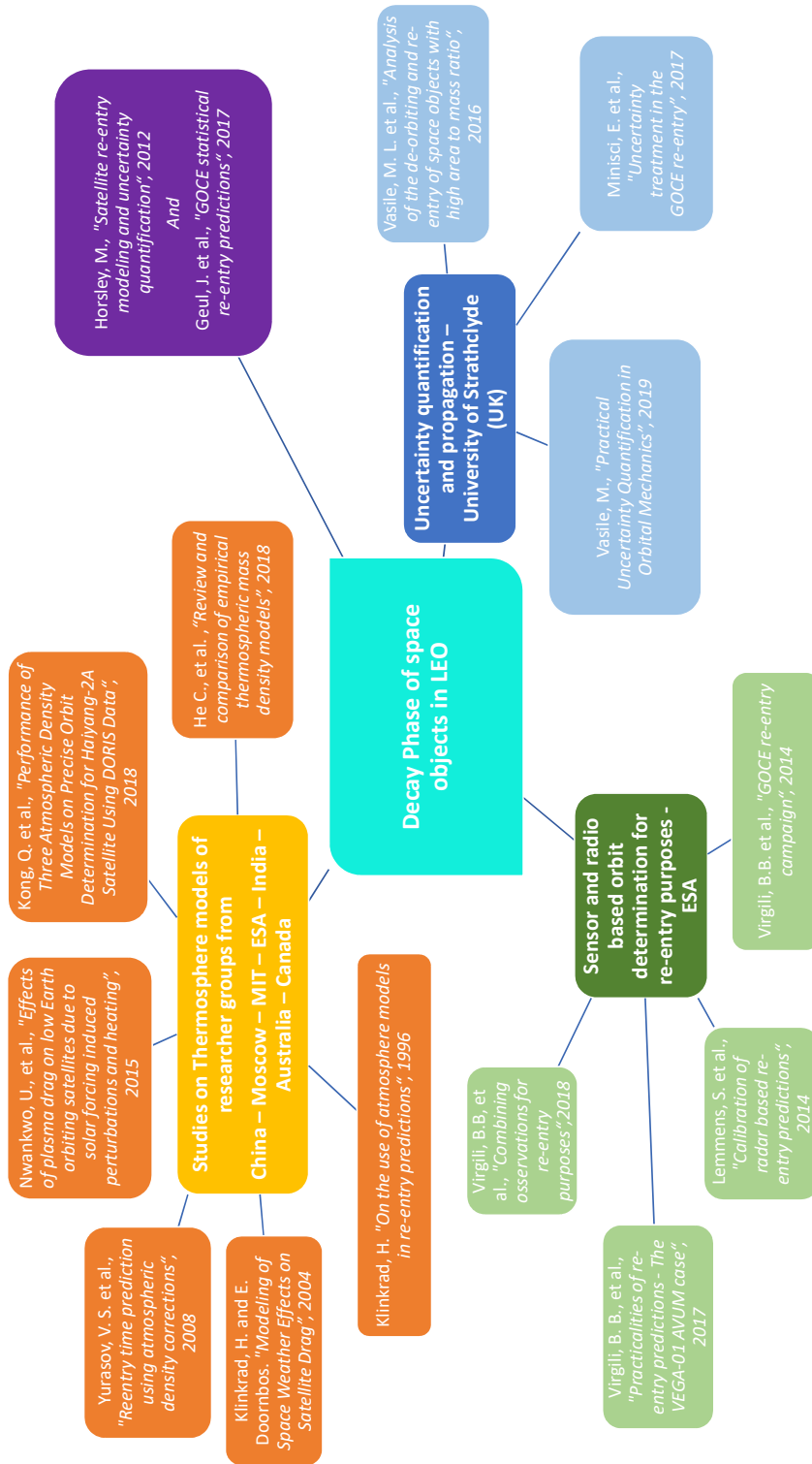


Figure 1.1. Schematic map of current literature

Thus, what emerges from the literature review is that there are still several issues during the re-entry phase. Substantially, the majority of these issues are commuted in uncertainties of the relative parameters due to a lack of knowledge about the phenomena at stake. Often, for this reason, the considered uncertainties are very large to be conservative. As it is reported in the lists of future steps above, one issue is common to every research area analysed and it consists of the uncertainty about the Thermosphere models. Currently, they cannot represent the thermospheric mass density (TMD) distribution and variability with enough accuracy as it would be required [2]. Usually, this is the main source of uncertainty in this kind of problem and this is one of the reasons for the unavailability of accurate orbit predictions in Low Earth Orbit (LEO), where the Thermosphere lies. The upper atmosphere is divided into three regimes [4]:

- The Homosphere (up to 90 km altitude) composed of Troposphere, Stratosphere and Mesosphere;
- The Thermosphere from 90 km to 300 km or 500 km depending on solar and geomagnetic activities;
- the Exosphere from the top of Thermosphere to space;

Analysing the decay phase of space objects in LEO, the Thermosphere is the one that needs to be modeled. To understand how the Thermosphere can influence the re-entry time windows the aerodynamic drag shall be introduced.

1.2 Aerodynamic drag

During re-entry the aerodynamic drag is the predominant perturbation acting on satellite and objects. Essentially, this is the result of the energy and momentum exchange between satellite and atmosphere [2]. This generates an aerodynamic force on the objects, that is possible to separate in Drag (in the opposite direction of the velocity) and Lift (perpendicularly to the drag, depending on the orientation of the object) [3]. Typically for spacecraft, the latter is usually orders of magnitude lower than the first one due to design choices. Drag acts opposite to the velocity allowing the free-fall orbit braking the spacecraft even if its velocity is increasing because it is attracted by the gravity field of the Earth. Moreover, the more the

drag rises the more re-entry time decreases. The drag’s acceleration can be modeled with the following law [2][3][6]:

$$a_d = -\frac{1}{2}\rho BC[\vec{v}_r]\vec{v}_r \quad (1.1)$$

where BC is the ballistic coefficient, ρ is the local TMD and \vec{v}_r is the relative velocity of the object with respect to the atmosphere which has a so-called velocity wind v_w . The ballistic coefficient is given by $BC = C_d \frac{A}{m}$ and contains already uncertainties. Firstly, the Drag coefficient (C_d) describes the interaction between atmospheric particles and satellite surfaces and depends on material, temperature and orientation of the surface. It depends on the temperature and composition of the atmosphere, too [5]. In the space environment, these parameters are not easy to predict and achieve, therefore C_d is often approximated in different ways and it is a source of uncertainty. For example:

- Usually, it can be assumed to be in a range [2.2 – 2.4] for orbit prediction of LEO satellites with a spherical shape [2] [6];
- To simplify the analysis, the spacecraft geometry can be modeled as a set of sphere, plates and cylinders, whose C_d can be known and the effective C_d can be estimated as a weighted sum of these three C_d through statistical coefficients [3];
- A data set of two-line elements (TLE) can be used as input in semi-analytical, e.g. ESA’s FOCUS, or numerical propagator, e.g. OrbGen to estimate ballistic coefficients in an iterative process trying to minimize errors through a linearly changing BC value [13];

Moreover, $\frac{A}{m}$ depends on the attitude of the spacecraft (if there is a 6 DoF analysis, otherwise the attitude is neglected) because the projected area varies consequently (there is an exception just in case the spacecraft is a sphere and the area is known). When the spacecraft re-enters, it has a certain velocity \vec{v} but the Earth is rotating and the atmosphere is co-rotating with the Earth with a velocity \vec{v} (usually neglected, or calculated from an empirical horizontal wind model [2]), hence the effective velocity to consider for the aerodynamic drag is the relative velocity $\vec{v}_r = \vec{v} - \vec{v}_w$. The last parameter influencing the aerodynamic drag is ρ . As it has been anticipated, this is the main source of uncertainty and it is the connection between the

thermospheric models and aerodynamic drag. This value can vary significantly with solar activity (solar irradiance, solar wind forcing) and with geomagnetic activity, therefore it is difficult to estimate and predict. Previous studies demonstrated these phenomena and stated that there is a significant heating and consequent expansion of the upper atmosphere during solar and geomagnetic activities [9]. In fact, during geomagnetic storms the atmosphere can be strongly heated by the interaction of the electromagnetic energy developed and the solar wind forcing (Joule Heating) which is the second most important index for this kind of problem [2]. Solar energetic events such as solar wind streams, coronal mass ejections (CMEs), solar flares and corotating interaction regions (CIRs) can cause atmosphere heating and in [9] it is demonstrated that intervals of strong solar or geomagnetic activity can increase decay rate in each event up to 60% depending on the severity and the duration of the event. Thermospheric models try to estimate these effects and an overview will be given in section 1.3.

1.3 Thermospheric indices and models

Generally, thermospheric models can be grouped into two categories [2]:

- Physical models which numerically solve the fluid equations of the coupled Thermosphere-Ionosphere system;
- Empirical models that capture the statistical behaviour of the atmosphere through a parameterised formulation;

Physical models require dedicated computation, thus empirical models are preferred for computational efficiency in orbital dynamics. For this reason, only empirical models will be analysed. They have been constantly updated in the years, because their modelling is based on multiple data such as TLE, ephemeris and ground-based and air-based measurements (e.g. neutral mass spectrometer, GNSS/GPS receivers, accelerometers etc). Therefore density, temperature, composition and total density of the atmosphere was found to vary with local solar time, day of the year, geographic longitude, geodetic latitude, daily solar flux index, a mean solar flux index on, typically, the previous three rotations of the sun (corresponding to 81 days) and usually daily geomagnetic index [4]. Overall, uncertainty lies in solar

and geomagnetic indices and in the difficulty of predicting them.

In order to provide an overview, the following list reports the solar and geomagnetic indices available in the literature [2]:

- $F_{10.7}$ is the daily indicator of the solar radio flux density at the wavelength of 10.7[cm]. The typical range is from $\sim 70[sfu]$ for low solar activity to $\sim 370[sfu]$ for the high one (the large variability is a reason for the related uncertainty). This is one of the most used indices in thermospheric models for its continuous long-term data sets and strong correlation with solar radiation and extreme ultraviolet radiation (EUV) which influences significantly TMD. The centered 81-day value is $F_{10.7}^-$;
- $MgII$ is the ratio of solar $MgII$ chromospheric core emission at 280 [nm] to the background solar wind continuum near 280 [nm]. It is mostly used when the main variable of interest of the thermospheric model is atmospheric temperature;
- $M_{10.7}$ is scaled from $MgII$ via a linear fit to $F_{10.7}$, in order to use it directly in the empirical models with the input of $F_{10.7}$. It is possible to have the 81-day value $M_{10.7}^-$, too;
- F_{30} is similar to $F_{10.7}$ but at the wavelength of 30 [cm]. It was found to be more sensitive than $F_{10.7}$ to longer wavelengths in ultraviolet (UV);
- $S_{10.7}$ is derived from the integrated EUV solar radiation at the wavelength of 26-34 [nm]. The 81-day value is sometimes used as $S_{10.7}^-$;
- $Lyman-\alpha$ is the solar flux index in Hydrogen $Lyman-\alpha$ transition wavelength of 121.57[nm]. Hydrogen $Lyman-\alpha$ is the main source of energy in lower Thermosphere during moderate and low solar conditions due to solar X-rays radiation;
- $E_{10.7}$ solar index is the integrated EUV flux density at the wavelength of 1 - 105 [nm]. It is demonstrated that $E_{10.7}$ is better than $F_{10.7}$ because the latter tends to overestimate the value of EUV radiance input to the atmosphere, hence $E_{10.7}$ is used in many latest models;

- $K - index$ is an integer quantifier for the geomagnetic field in the range from 0 to 9. If $K - index \leq 1$ there is calm geomagnetic conditions, otherwise if $K - index \geq 5$ there are disturbed conditions;
- a_p and K_p indices are daily 3-h planetary geomagnetic indices with different scales. K_p is derived from the 3-h $K - index$ and it is possible to define A_p as the daily mean value of eight a_p ;
- a_m and K_m are 3-h indices and the first one is derived from $K - index$ computed at a network of observatories located in nine different longitude sectors in order to give a good representation of the energy input to the magnetosphere. K_m is a quasi-logarithmic value of a_m but often they are not used;
- There are several solar wind indices such as flow pressure, flow temperature, flow speed, interplanetary magnetic field (IMF), etc. and others are determined on multiple observations and they are another important input;

Generally, thermospheric models use a similar set of input parameters including at least time of the day, current year, altitude, geographic location, a solar flux index as $F_{10.7}$ and a geomagnetic index as a_p or K_p [4] [5] [6]. These inputs were selected by the models' developers because they were the best available choice due to their good correlations with the observed density variations and their availability in long time-series with historical density and temperature datasets. Usually, these measurements are ground-based data and by their nature, they cannot give a complete picture of what is happening at spacecraft altitudes. Therefore, over the years accelerometers and tracking data were included in the models increasing the accuracy [1] [5] [6] [13]. However, variations in density are still too complex to modeling accurately and typical error related to atmospheric density with these models is about 15%. There are several categories of thermospheric models developed over the years and an overview is given in [2]:

- *Jacchia-class* models give as output atmospheric temperature, TMD, pressure and concentrations of the six main atmosphere components (N_2 , O_2 , Ar , He , O , H) for the altitude in the range from 90 km to 2500 km. The construction of these models is essentially the same and they derive TMD from an empirical temperature profile calculating the concentration (number

density) of each component n_i as a function of geometric height z by numerically integrating the diffusion equation. There are three models (Jacchia70, Jacchia71, Jacchia77) but the most used model of this class is Jacchia71 which was incorporated into the Committee on Space Research (COSPAR) International Reference Atmosphere 1972 (CIRA-1972). Jacchia70 cannot predict the diurnal variation of TMD. Jacchia71 has still some limitations estimating the variation of TMD in a period less than one day and every model of this class overestimates TMD due to drag coefficient of 2.2 used but it is still very used actually and it is a sort of reference for other models.

- *MSIS-class* models were implemented for the first time as MSIS83 and over the years it evolved in MSIS86 (improved precision over the polar region), MSIS90 (lower altitude boundary extended to Earth surface) and finally in NRLMSISE00. The last one is the most used of this class and cover an altitude range from the Earth surface to 1000 km. It is based on a particular neutral temperature profile of the Thermosphere and it takes into account the polynomial terms with solar activity indices, linear and exponential terms with geomagnetic activity indices, spherical harmonics terms and time-dependent periodic terms in time of the day and day of the year. Moreover, it estimates the anomalous oxygen (O^+) which influence the atmospheric drag, too. Actually, this is one of the most important model of Thermosphere and it is often used in typical applications, e.g. [9] [13] [15].
- *JB-class* models (Jacchia-Bowman) were developed from Jacchia71. Essentially, the former adopts more solar indices and geomagnetic indices than the latter. In JB2006, $S_{10.7}$ and $MgII$ are used as inputs to estimate solar irradiance in the EUV and UV wavelengths. Furthermore, D_{st} is used in JB2008 to account for geomagnetic activity effects on exospheric temperature.
- *DTM-class* models (Drag Temperature Models) were developed for the first time in the version of DTM78 by CNES/GRCS (Center National d'Etudes Spatiales/Groupe de Recherches de Géodésie Spatiale). They use a different modelling of the concentration of the components n_i which are approximated with an exponential function as for the *MSIS-class* but scaled with an additional function of altitude. The evolution of this class of models is based on the

implementation of new measurements and/or methodologies: DTM94 incorporated calibrating factors to adjust drag measurements of different satellites, DTM2000 added *MgII* index to the inputs, DTM2009 was updated with accelerometers measurements from both CHAMP and GRACE satellites to take into account horizontal variations and lastly DTM2012 and DTM 2013 included new measurements such as four years of GOCE-derived TMD data for DTM2013.

- *GAMDM-class* models (Global Average Mass Density Model) use a catalog of TLE data of 5000 near-Earth space objects between 1967-2007 to estimate the global long-term trends in TMD. GAMDM models are time-dependent and TMD is described with a more complex logarithmic equation. These models are limited to the daily-mean value of TMD at specific altitudes.
- *MET-class* models were implemented by NASA Marshall Space Flight Center. The first model was created in 1988 but it was not accurate due to errors in the numerical integration algorithm. Its evolutions in 1999 and 2007 considered the solar position (1999) and the seasonal and latitudinal variations in TMD below 170 km and above 500 km, both updated from Jacchia71.

Other classes of models are available in the literature (e.g. *GRAM*, *DCA* and accelerometer derived models) but limited information are given and they are not so used as the ones mentioned above.

1.4 Brief overview of orbit propagators

The last element in this kind of studies is represented by the orbit propagator, used to achieve a re-entry time windows for the selected object from defined initial conditions. There are many ways to propagate an orbit depending on the needs and on the desired accuracy of the model. Typically, they can be distinguished in two main categories: 3 degrees of freedom (DoF) propagators and 6DoF propagators. Within these categories, there are several numerical methods to propagate the orbit depending on the boundary conditions of the problem. These methods are necessary because the propagation consists of an integration of the motion equations

(perturbation included). Therefore, it is necessary to know the ordinary differential equations and the initial conditions which describe the problem. Essentially, the 3DoF propagator considers just the reference surface and the Mass of the object without the attitude and this is the reason why the object is assumed to be modeled as a sphere. The object is not affected by the aerodynamic stability and its motion is assumed to be randomly tumbling, hence only Drag is considered while the Lift is neglected. The state vector is composed of 6 components: 3 for the position vector and 3 for the velocity vector, both in the ECI (Earth-Centered Inertial) coordinates. On the other hand, if there is a dependency of the orbital motion on attitude a 6DoF higher fidelity analysis is required. This is much more computationally expensive than the previous one, but it is necessary to analyse certain problems. Usually, attitude is represented by quaternions and the complete state is represented by 13 state variables: position, velocity, attitude quaternion and rotational rate in the body-frame [1] [8] [11].

Since a 6DoF analysis was unnecessary and computationally too expensive, in this work a lower fidelity 3DoF propagator has been used and it will be presented in section 2.3.

Chapter 2

Modelling Phase

2.1 Thermosphere Model

Generally, the first step to modeling this kind of problem is the choice of the Thermosphere model to analyse. As reported in chapter 1, there are several Thermosphere models that have been developed over the years. However, the NRLMSISE00 has been selected as the most suitable one for this work. The main reasons are that it is the most commonly used as reference model in the last years, it includes the majority of the effects which are present in the Thermosphere and above all it is an open-source model which is already implemented as a function in the MATLAB *Aerospace Toolbox*, too. It is comfortable to use and the function is called *atmosnrlmsise00*. It requires the following inputs:

- Altitude [m];
- Latitude [deg];
- Longitude [deg];
- Year;
- Day of the year;
- UT seconds in the day;

- The 81-day average of $F_{10.7}$ flux centered in the day of the year $F_{10.7}^-$ (below 80 [km] of altitude this effect is not large and it is considered as a constant value of 150 [sfu]);
- The daily $F_{10.7}$ value (as for the 81-day average below 80 [km] the default value is 150 [sfu]);
- An array of 7 a_p magnetic index information (daily a_p , 3-hour a_p for the current time, 3-hour a_p for 3 hours before the current time, 3-hour a_p for 6 hours before the current time, 3-hour a_p for 9 hours before the current time, average of 3-hour a_p from 12 to 33 hours before the current time and average of 3-hour a_p from 36 to 57 hours before the current time) that below 80 [km] has a default value of 4 for the same reasons of the solar indices;
- There is also the opportunity to take into account the effect of the anomalous oxygen (O^+) calculating TMD specifying 'Oxygen' as input;

About this work, the most important output of this function is the TMD in $[\frac{kg}{m^3}]$ but it can give more output as the temperature at the specified altitude or the density of each component of the Thermosphere¹. Concerning the inputs of the thermospheric model, it has been decided to investigate how the uncertainty in the prediction of the solar and geomagnetic indices values influences the re-entry time windows of specific space objects (chapter 4). In fact, as it emerges from the literature review the lack of real data for the future values of the indices is a very important open point.

2.2 Prediction of the indices

The prediction of the indices necessary as inputs in the model previously mentioned is based on historical data collected by the *National Oceanic and Atmospheric Administration* (NOAA)². The catalogues of the geomagnetic indices (daily A_p and the correspondent 3-hour values) were provided by *Helmholtz Centre Potsdam GFZ*,

¹See <https://www.mathworks.com/help/aerotbx/ug/atmosnrlmsise00.html>

²<https://www.ngdc.noaa.gov>

while the catalogues for solar indices (daily $F_{10.7}$) were provided by the *National Research Council of Canada (NRCC)* through daily ground observation at *Algonquin Radio Observatory*, near *Ottawa (Canada)* until 1991 and at *Dominion Radio Astrophysical Observatory*, near *Penticton (Canada)* from June 1, 1991. The values are available until 30/04/2018, hence the target is to predict future indices after this date. In order to accomplish it, a time series analysis shall be conducted.

Facebook Prophet has been identified as a useful tool to achieve it. *Prophet* is a forecasting open source software based on an additive model where non-linear trend are fit through specific seasonality. The procedure is available in *Python* or *R* and *Python* has been considered as the best programming language to write the code. However, there is no difference running it with *Python* or *R* because the procedure is the same. Moreover, it is really user-friendly and essentially it is composed of two main parts. The first one is based on importing *.csv* files about historical data the user wants to predict (in a specified format composed by two columns with *'ds'* containing datestamp in the format YYYY/MM/DD and *'y'* containing the measurements) and on fitting the data with a *Prophet* model with specified parameters (e.g. helping *Prophet* to catch the trend and to find the seasonality if there is one). The second one consists in specifying the parameters about the desired future data frame and the days that *Prophet* shall predict, then it is possible to create the forecast model and to predict the values. The results are available creating another *.csv* file through the classical routines of *Python* and it contains essentially four columns:

- The future datestamp *'ds'*;
- The predicted values of the measurements *'yhat'*;
- The upper *'yhat_upper'* and lower *'yhat_lower'* values of the uncertainty related to the *'yhat'* forecasting for every date;

It is also possible to export this *.csv* file and to show the results through plots displaying the *change-points* (the points where *Prophet* catch the trend variation).

Concerning this work, several tests have been carried out in order to find the right combination of parameters to allow *Prophet* to fit the model and to give a reliable forecast. The prediction of solar and geomagnetic indices requires different considerations due to their distinctive nature.

2.2.1 Prediction of daily $F_{10.7}$

The solar indices are related to the solar cycle, therefore the values of $F_{10.7}$ depend on the solar activity (chapter 1). The solar cycle lasts eleven years and it is the sun's magnetic field cycle. Displaying the measurements of $F_{10.7}$ over the years in *Prophet* through the fitting model, it is clear that the trend follows this cycle with oscillations of different amplitude. The catalogues of the solar indices collect values from 1965. For the first tests, just the values after 2005 and the default settings of *Prophet* were used in order to learn how the software works. The prediction was until the end of 2021 and as the figure 2.1 shows the result is not satisfying. Even the fitting is not satisfying: empirical data is represented by the black points

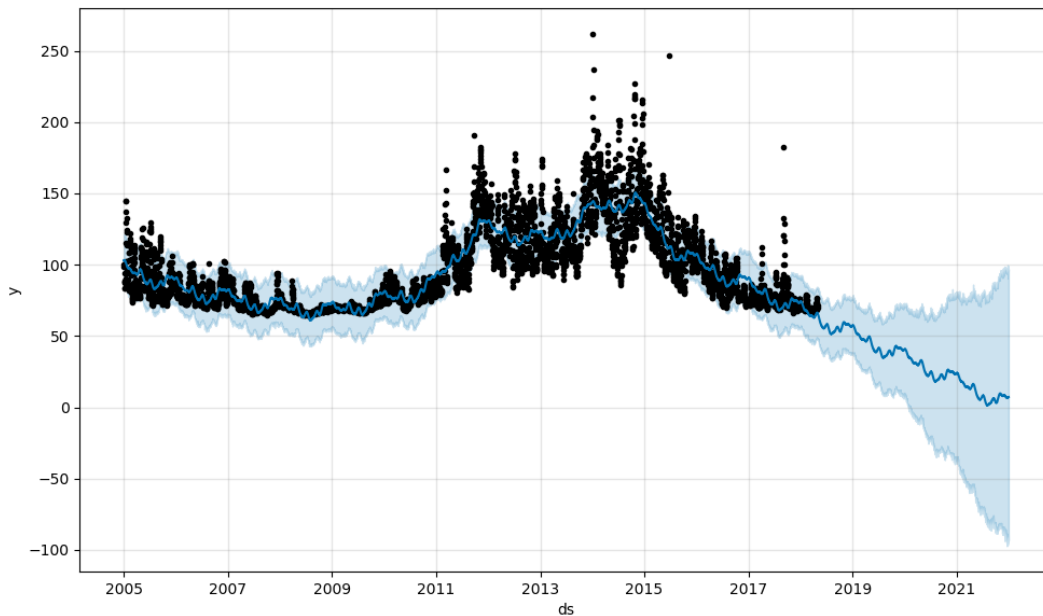


Figure 2.1. First test: fitting solar indices from 2005 to the 30/04/2018 and forecasting values until the end of 2021

while the light blue band represents the range of uncertainty or confidence interval. Overall, there is an asymptotic trend in the future values and in fact, the mean value (represented by the dark blue line) tends to negative values, which is not possible. The reasons for this bad result lie in the default settings of *Prophet*. It is necessary to well understand how they influence the results and to adapt them to this problem. Here, some of them are summarised:

- Changepoint range (the range of the historical data used from the fitting model in order to "learn the trend") is usually set to 80%;
- There are weekly and yearly seasonality, but in this case, they are useless because the only seasonality influencing the results is the solar cycle;
- The regression model has a linear growth (the logistic model is also available but it is used more in order to limit mean values with higher and lower boundaries);
- The default value for the width of the interval of uncertainty (confidence interval) is 80%;

There are many more settings but the ones reported above shall be changed properly because their influence on the results is relevant. Moreover, there are still some good norms to follow dealing with tools like *Prophet*:

- In order to catch a seasonality, many years of measurements are necessary (at least three complete cycles);
- The fitting model will never include every empirical data, because there are peaks in the values of these indices that are related to particularly strong solar phenomena (for example solar eruption) which are considered as noise by *Prophet*. However, these peaks are impossible to predict and a fitting model is considered satisfactory when it includes the majority of the empirical data;
- If the period to forecast increases the uncertainty interval increases too, hence it is better to forecast a range of years pertinent to the range of used empirical data;

Therefore, several actions have been performed based on the conclusions reported above in order to achieve better predictions. Since the future values are obviously unknown, tests were carried out on ranges of past data (getting a kind of cross-validation) by varying ranges of empirical data, periods to forecast and settings used in *Prophet* in order to understand which actions could bring benefits and which were useless. Considering only the solar indices, forty-two tests were realised and just the most important conclusions are reported below:

- First of all, empirical data has been pre-processed switching to a natural logarithmic scale of measurements. This trick allowed to compact the data, obtaining a better fitting model due to the decrease of the noise as it is possible to see in figure 2.2;
- As it is possible to see in figure 2.1 and 2.2, there is an asymptotic behavior of the mean predicted value. The main reason is that *Prophet* can't identify the solar cycle seasonality by itself. In order to fix this problem, the weekly seasonality has been turned off and a new seasonality with period 4015 days (neglecting leap years, 4015 days are equivalent to eleven years) has been added;
- As it is reported in the good norms above mentioned, a so long seasonality implies that the number of the years to consider shall be much higher (approximately three solar cycle, hence thirty-three years at least);
- To be sure that *Prophet* can recognize the real trend of the historical data without missing some points, the changepoint range was set to 98%. The effect of the last three actions can be observed in figure 2.3, where the red vertical dashed lines are the changepoints (points where the trend changes). It is also possible to observe that it is really hard to predict several years (in this case ten years using a data frame of thirty-four years) because the interval of uncertainty tends to increase too much, as expected. Considering the data frame of empirical past data available, a good compromise has been identified in predicting four years;
- In conclusion, the confidence interval was increased to 90% in order to predict the future values of the indices as much as possible keeping reasonable computational times. In fact, a comparison among different values of confidence intervals (80%, 90%, 95%) is reported in figure 2.4. Mean values are better with confidence intervals equal to 90% and 95%, while with 80% the curve is too steep. In fact, the 80% case shows in figure 2.5 that when the period to forecast is expanded it reaches too high values. Moreover, it is better to consider higher confidence intervals because the predictions will be more reliable. Concerning the 90% and 95% cases, the last one includes an higher range of values but they are useless because as it is possible to note from the

past data it considers values that have never been observed. In fact, values of $F_{10.7}$ above 6.0 (in the natural logarithmic scale, so they correspond to about 403[sfu]) and below 4.0 (corresponding to about 54[sfu]) have been neglected in this work and for these reasons the confidence interval was set to 90%;

The result of all these operations (summarised in table 2.1) is reported in figure 2.6, which correspond to the top right plot of the figure 2.4 and it was found to be a satisfying outcome. Therefore, a new catalogue of the $F_{10.7}$ solar index from 01/05/2018 (first predicted value) until the end of the 2021 was created exporting a *.csv* file from *Prophet*, where higher values of 400[sfu] were limited to 400[sfu] and lower values than 50[sfu] were limited to 50[sfu]. In the simulations reported in chapter 4, the catalogues start from the beginning of 2018 and the first 120 values until 30/04/2018 are the real values (the upper and lower boundaries are estimated with the fitting model).

Operations for prediction of Solar Index $F_{10.7}$	
Past data	From 1980 to 30/04/2018
Pre-Processing Data	Switch to the natural logarithmic scale
Seasonality	Solar Cycle (11 years)
Changepoint range	98%
Interval Width	90%
Post-Processing Data	Limiting values between 50[sfu] and 400[sfu]

Table 2.1. Operations to obtain the catalog of the future $F_{10.7}$ indices

2.2.2 Prediction of daily 3-hour a_p

First of all, it is necessary to specify that every 3-hour a_p index (a_{p0-3} , a_{p3-6} , a_{p6-9} , a_{p9-12} , a_{p12-15} , a_{p15-18} , a_{p18-21} , a_{p21-24} , where the numbers represent the hours in UT to which the indices refer) has been predicted separately using catalogues of each index over the years due to the format required by *Prophet* and already specified above.

However, the behavior of these indices is different compared to the $F_{10.7}$. Actually, they are not influenced by a cycle and it seems that there is no seasonality. Moreover, typical values vary from 0 to 40 in relatively calm conditions, but they can reach higher values (even up to 400) when there are geomagnetic storms. As it happens

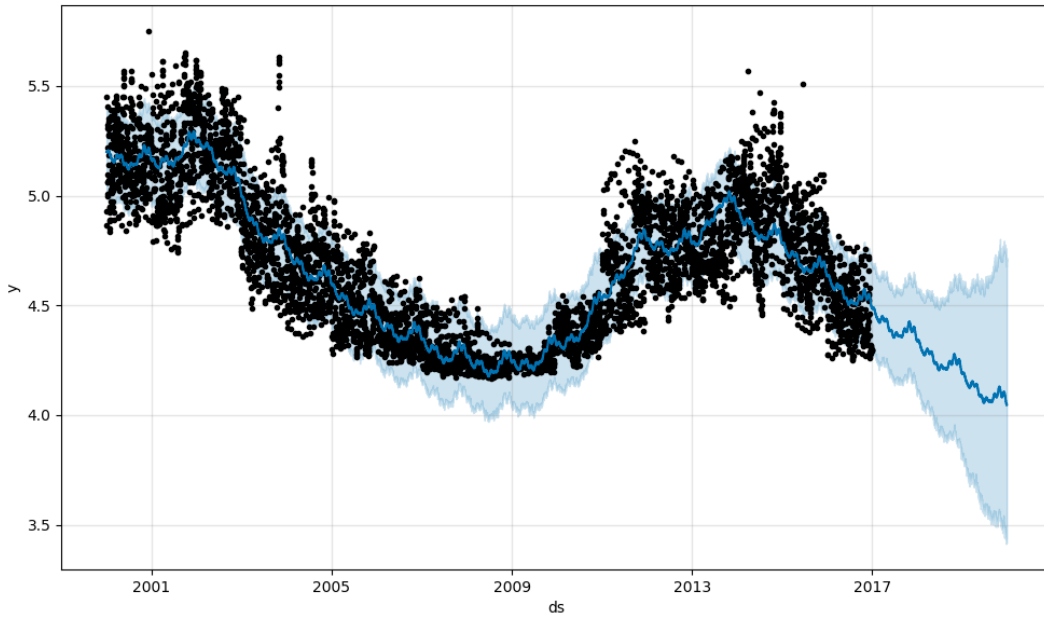


Figure 2.2. Fitting solar indices from 2000 to the end of 2016 and forecasting values until the end of 2019

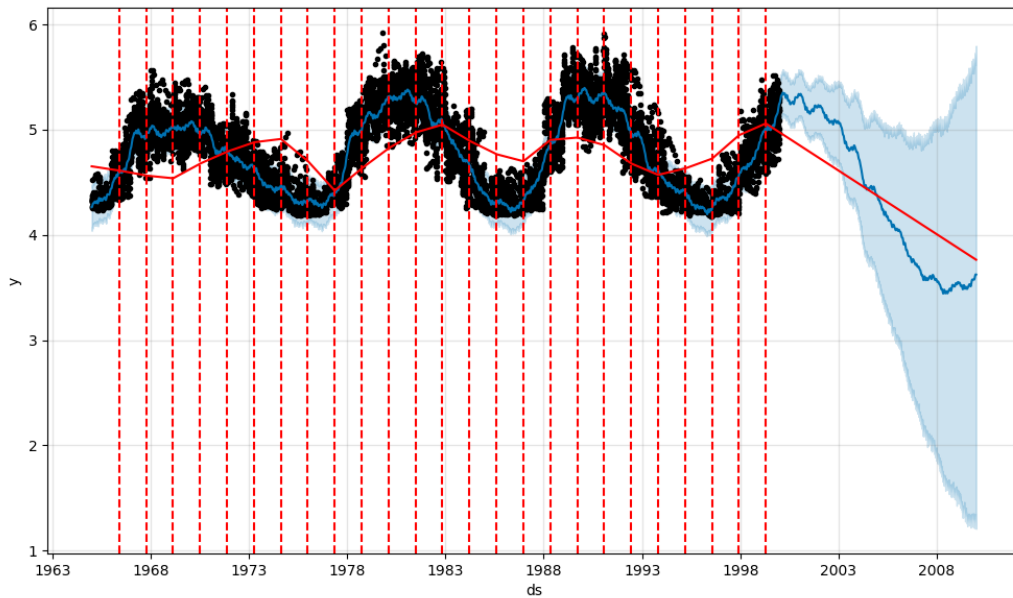


Figure 2.3. Fitting solar indices from 1965 to the end of 1999 and forecasting values until the end of 2009

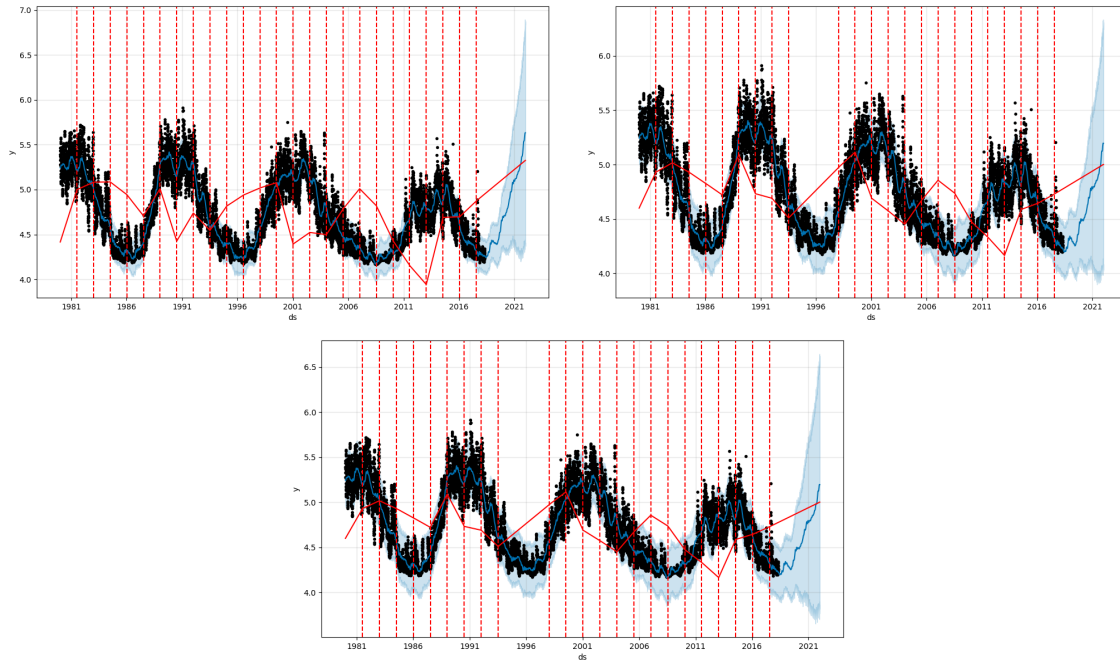


Figure 2.4. Comparison among different confidence intervals (the top left is set to 80%, the top right is set to 90% and the one below is set to 95%)

for the solar indices, these peaks are considered as noise by *Prophet* and they are neglected. The main problem in this situation is that it is really hard to find a trend to follow, as it is possible to view in figure 2.7 which refers to a_{p0-3} with the default settings of *Prophet*.

Another issue is that the lower value of the predicted range of geomagnetic indices can reach negative values. In order to solve that, a logistic growth trend model has been adopted during the forecasting process (the default model in *Prophet* is the linear growth). Usually, this kind of model is used with binary values but it is useful in this case because it forces the predicted mean values to remain in the defined limits (Figure 2.8). The confidence interval can still include values outside the limits and for this reason the exported *.csv* files of the 3-hour a_p need to be post-processed, replacing every negative value with zero.

Since geomagnetic activity doesn't follow a cycle and there is not a predominant trend, it has been considered unnecessary taking several years of past data as for the solar indices. However, in order to ensure an appropriate forecasting model, the confidence interval has been increased to 90% and the changepoint range has been

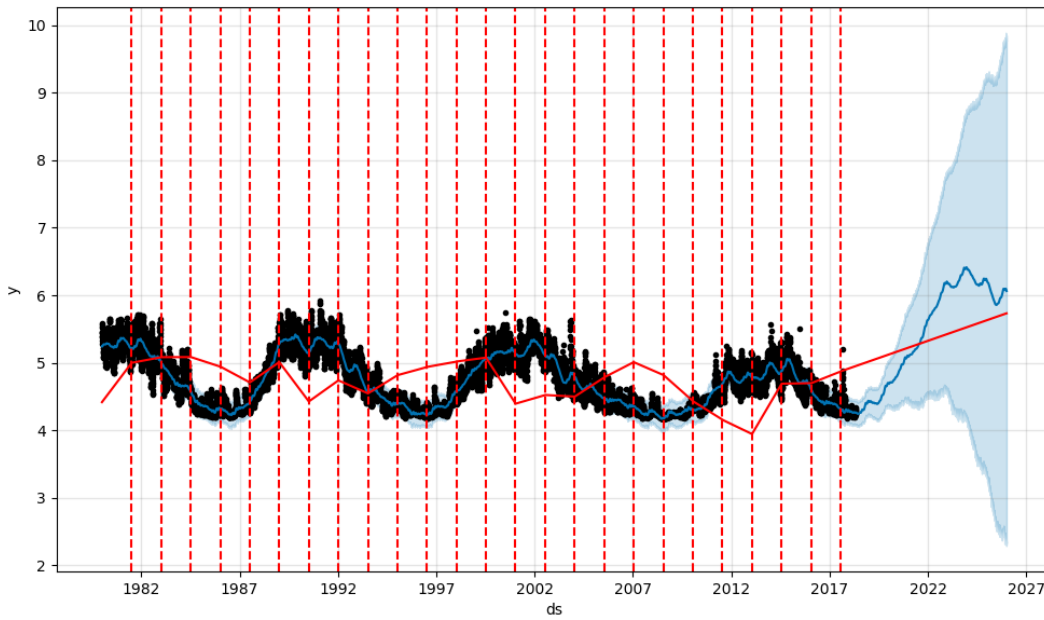


Figure 2.5. Fitting solar indices from 1980 to 30/04/2018 and forecasting values until the end of 2025

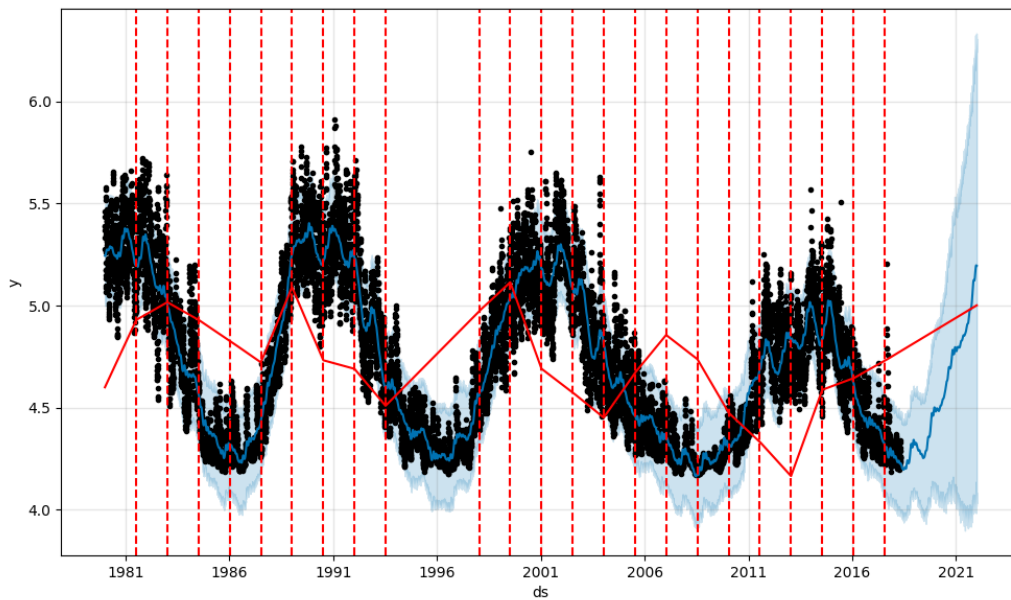


Figure 2.6. Best result: fitting solar indices from 1980 to 30/04/2018 and forecasting values until the end of 2021

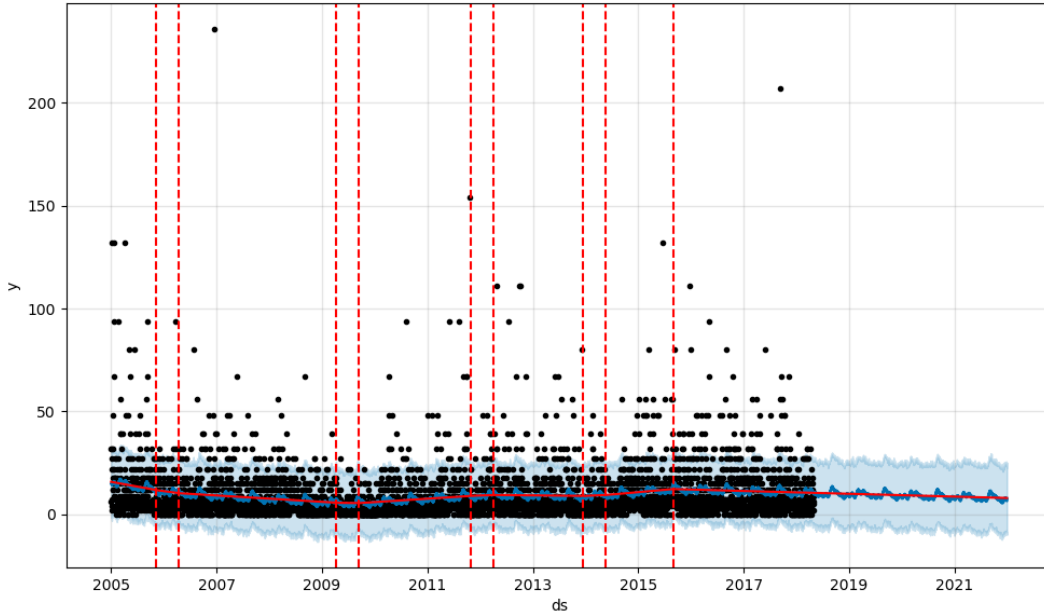


Figure 2.7. Fitting geomagnetic index a_{p0-3} from 2005 to 30/04/2018 and forecasting values until the end of 2021 with default settings of *Prophet*

expanded to 98%. The adopted settings are summarised in table 2.2 and the result for the a_{p0-3} index is reported in figure 2.9, followed from all the remaining seven a_p indices from figure 2.10 to figure 2.16.

Operations for prediction of Geomagnetic Indices 3-hour a_p	
Past data	From 2005 to 30/04/2018
Growth model	Logistic
Changepoint range	98%
Interval Width	90%
Post-processing	Replacing negative values with zero

Table 2.2. Operations to obtain the catalog of the future a_p indices

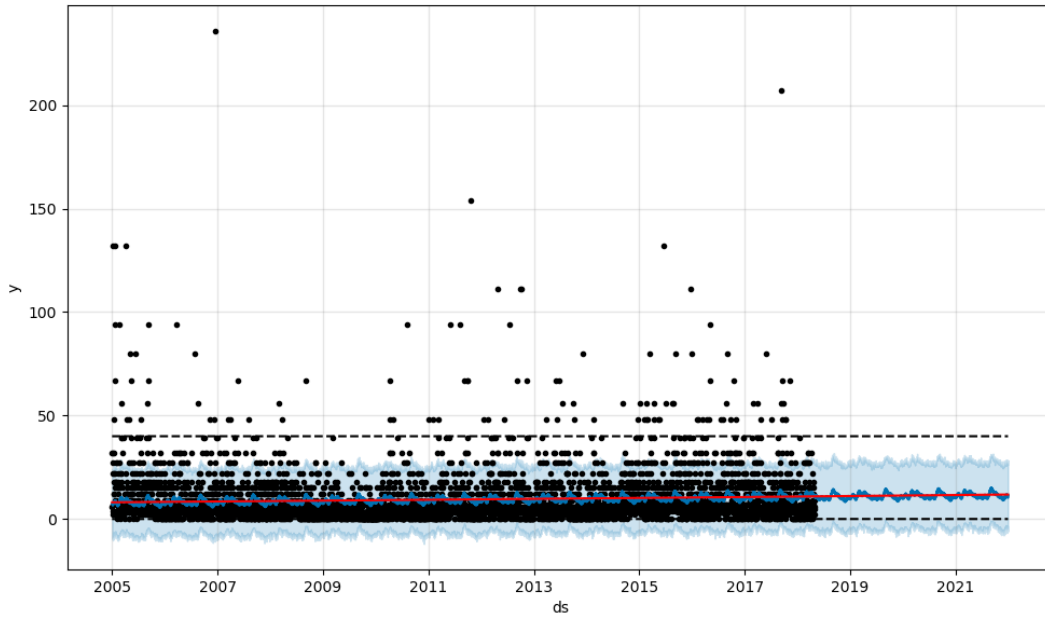


Figure 2.8. Fitting a_{p0-3} from 2005 to 30/04/2018 and forecasting values until the end of 2021 with logistic growth (limited between 0 and 40)

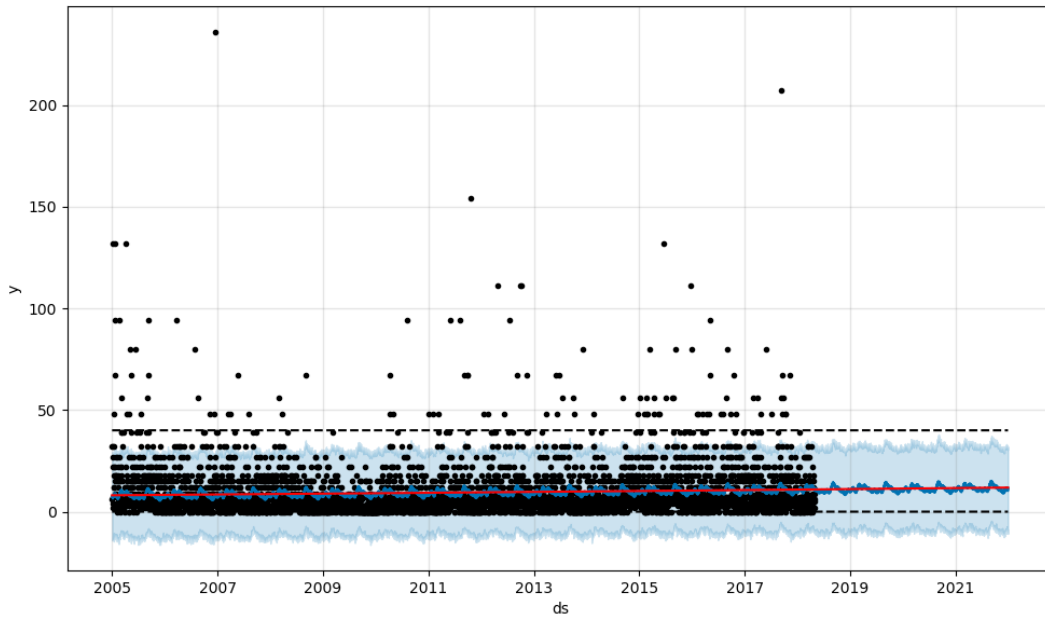


Figure 2.9. Fitting geomagnetic index a_{p0-3} from 2005 to 30/04/2018 and forecasting values until the end of 2021

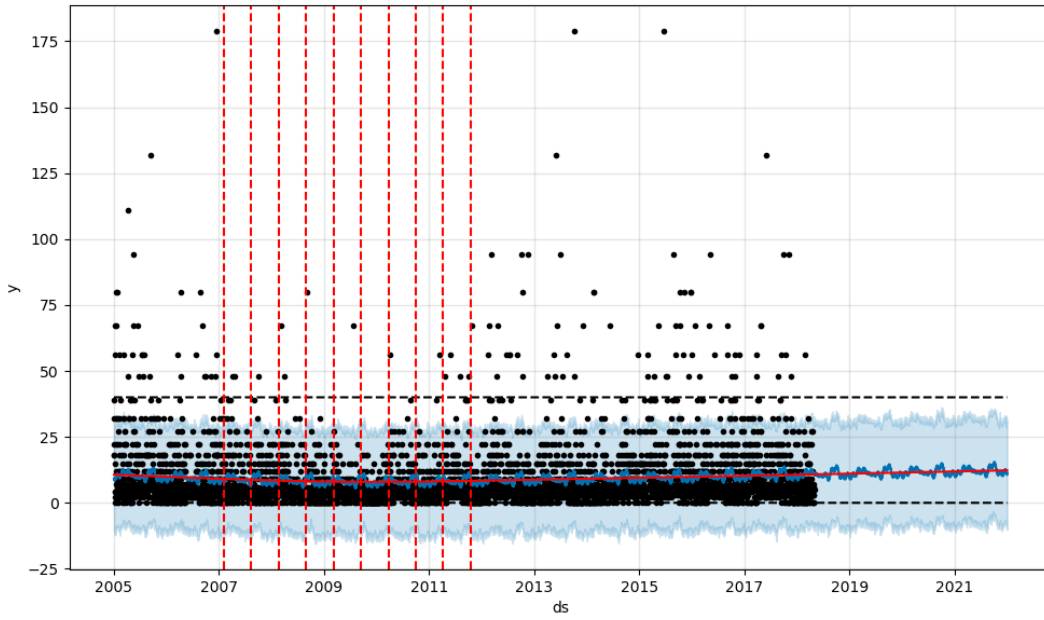


Figure 2.10. Fitting geomagnetic index a_{p3-6} from 2005 to 30/04/2018 and forecasting values until the end of 2021

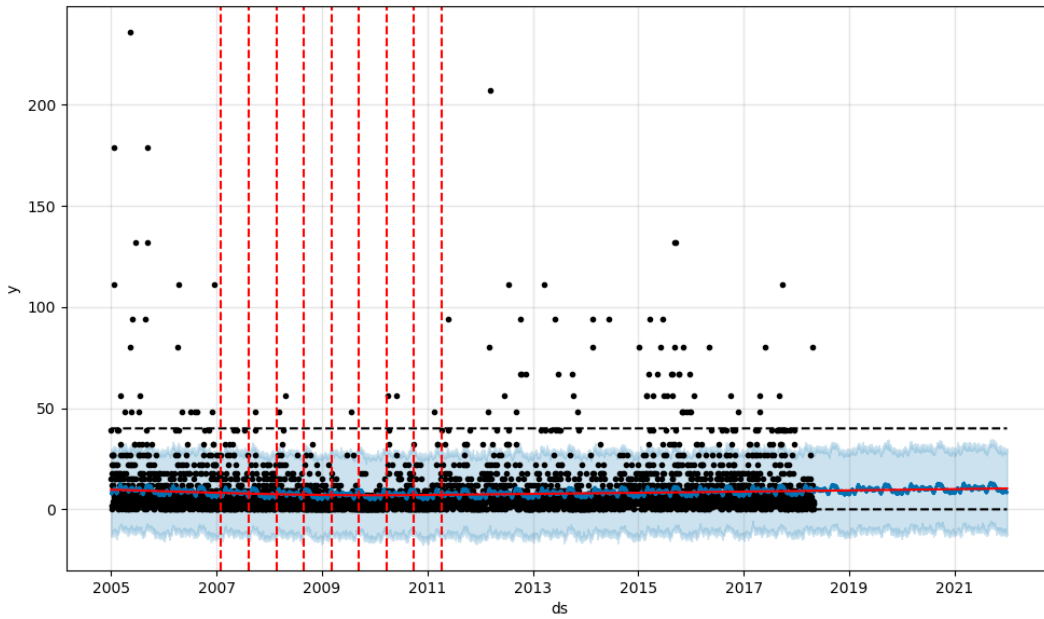


Figure 2.11. Fitting geomagnetic index a_{p6-9} from 2005 to 30/04/2018 and forecasting values until the end of 2021

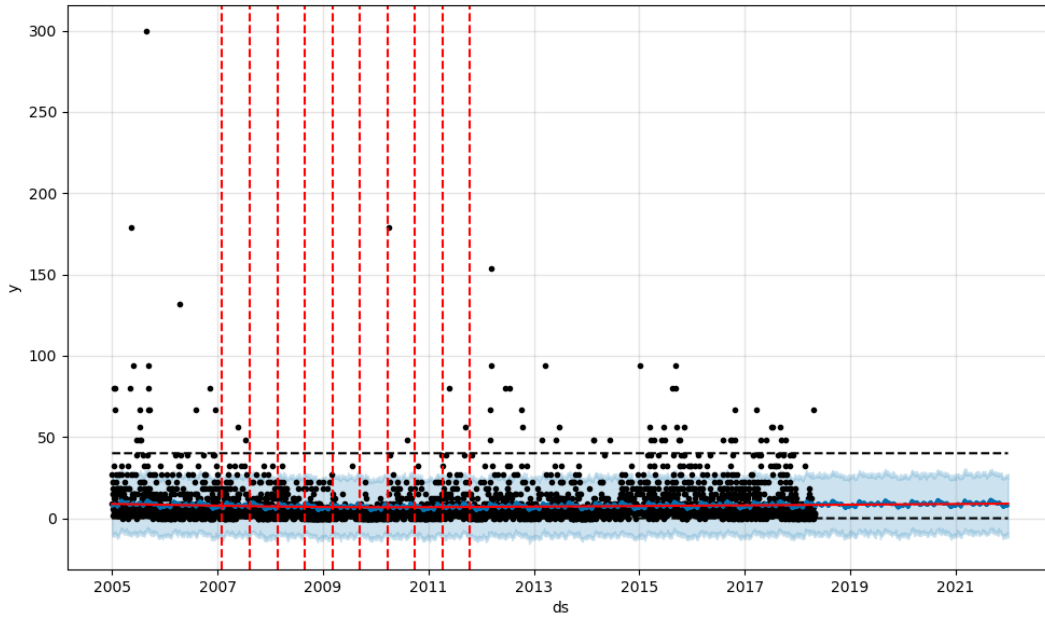


Figure 2.12. Fitting geomagnetic index a_{p9-12} from 2005 to 30/04/2018 and forecasting values until the end of 2021

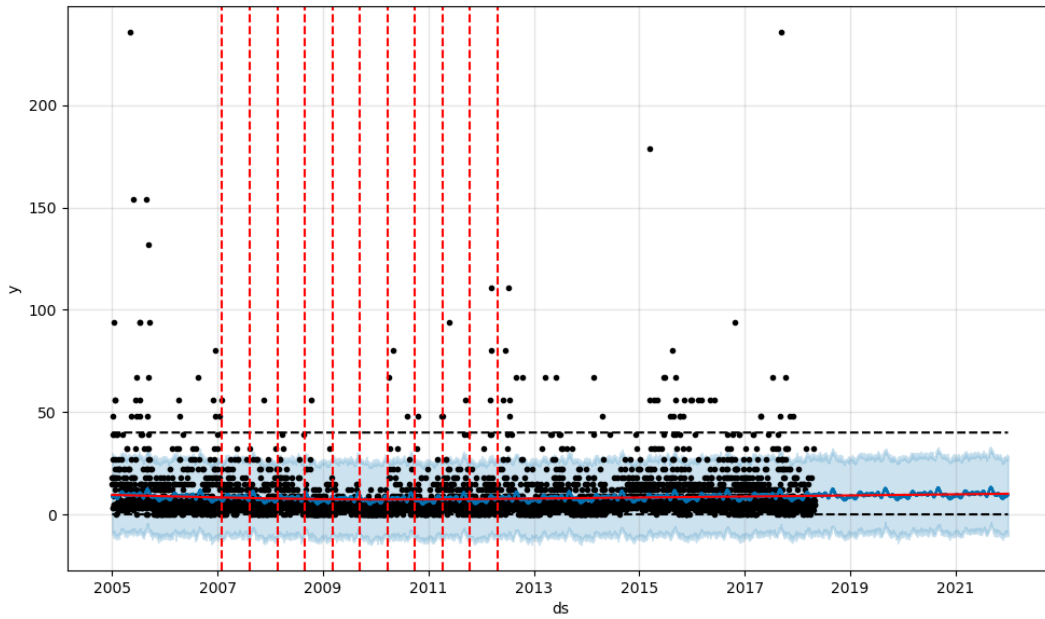


Figure 2.13. Fitting geomagnetic index a_{p12-15} from 2005 to 30/04/2018 and forecasting values until the end of 2021

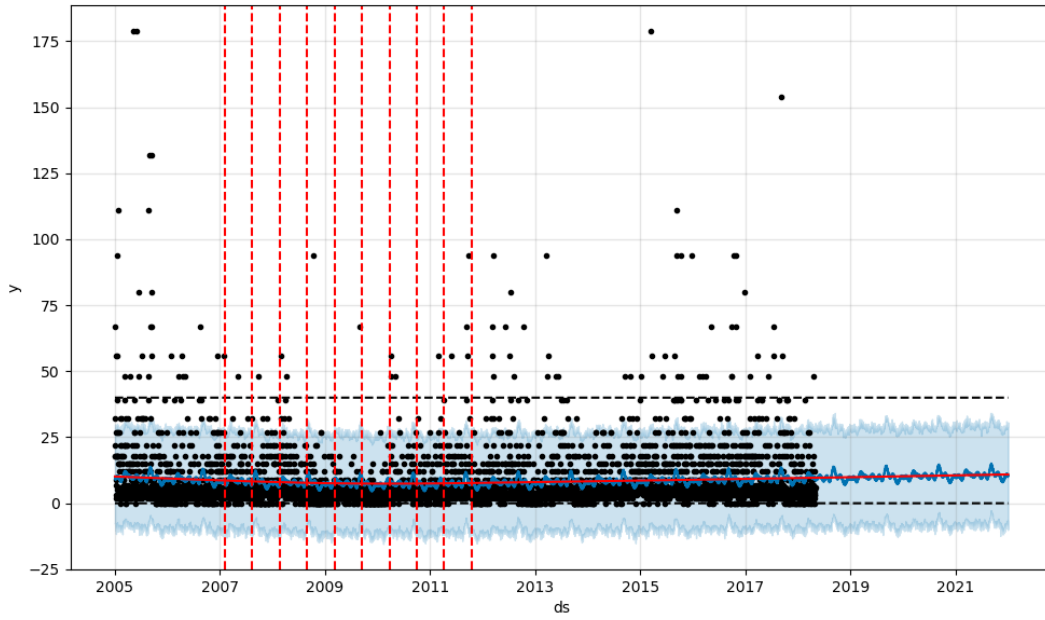


Figure 2.14. Fitting geomagnetic index a_{p15-18} from 2005 to 30/04/2018 and forecasting values until the end of 2021

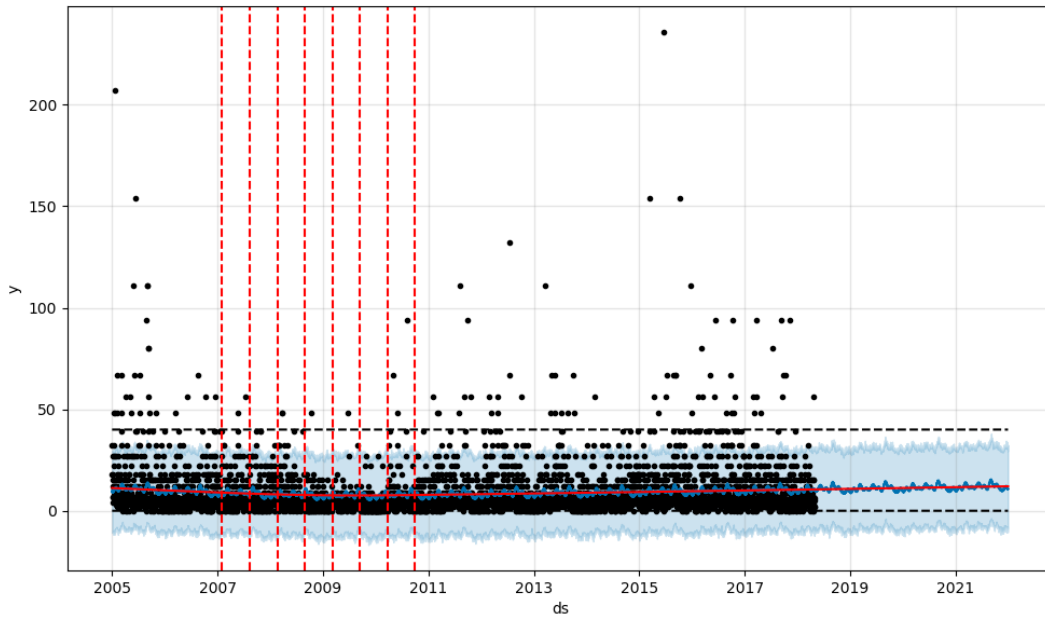


Figure 2.15. Fitting geomagnetic index a_{p18-21} from 2005 to 30/04/2018 and forecasting values until the end of 2021

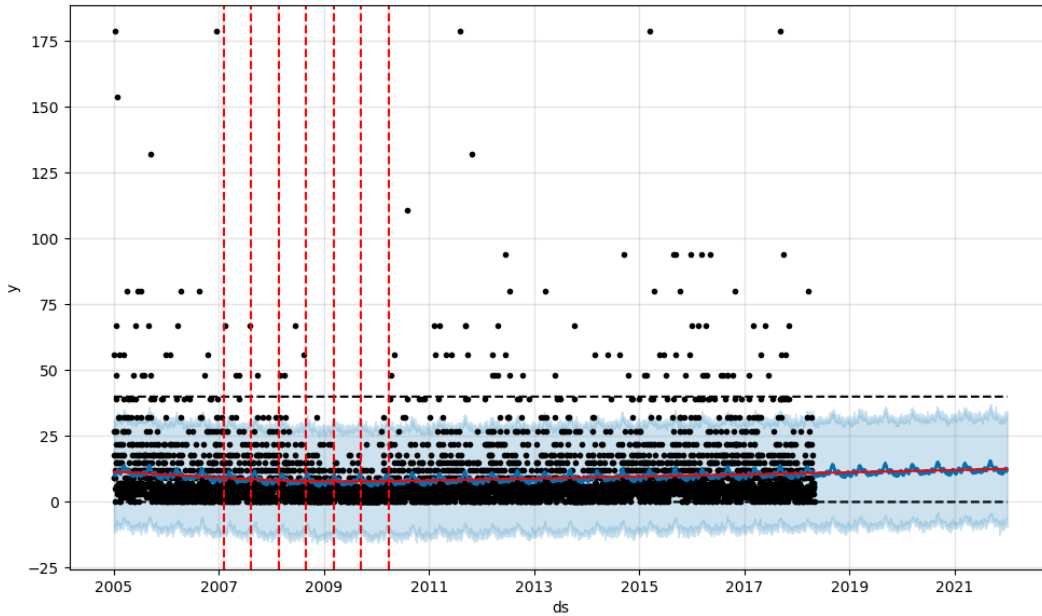


Figure 2.16. Fitting geomagnetic index a_{p21-24} from 2005 to 30/04/2018 and forecasting values until the end of 2021

2.3 Calculation of re-entry time window

2.3.1 Identifying maximum and minimum TMD

Once the indices are predicted, it is all set for the calculation of the re-entry time windows. The term "re-entry time windows" is referred to the difference between the minimum and the maximum re-entry time. The reason lies in the prediction of the indices. It is impossible to predict a deterministic value of them, but they are estimated within a range of values as it has been illustrated in the previous section. However, *Facebook Prophet* doesn't specify how the probability is distributed in this range. For this reason, at the beginning an optimization of TMD by varying the solar and geomagnetic indices between upper and lower boundaries given by *Prophet* has been performed since the Thermosphere model could have non-linearity in the distribution of the TMD. The optimization was performed with the function *fmincon* already implemented in MATLAB. This function looks for the minimum of the specified objective function output (the TMD in this case) and the same function can be used to look for the maximum value just minimizing the inverse function.

Obviously, the function which contains the Thermosphere model is inside the objective function specified in the optimizer and during the optimization only the input relative to the indices are supposed to vary while every other input is considered constant. The typical values of TMD at altitudes above 100 [km] can be really low if expressed in $[\frac{kg}{m^3}]$ (even $10^{-8} - 10^{-12}$). For this reason, the tolerances of the optimizer have been set to 10^{-7} and the values of TMD inside the optimizer have been transformed in $\frac{kg}{km^3}$ in order to have higher values and avoid numerical problems. In this way, an estimation of the maximum and minimum TMD values is achieved. However, *fmincon* can display the value of the indices which give the minimum or the maximum searched value (depending on the simulations) as a further output. Testing the optimizer, it immediately emerged that the minimum and maximum values found with *fmincon* were identified always in proximity of the lower and upper boundaries of the solar and geomagnetic indices. This has led to the conclusion that the Thermosphere model could have a linear relationship with the solar and geomagnetic indices. This has been verified with a simple test. First of all, it has been decided a set of inputs for the NRLMSISE00 model with constant values choosing a fixed point in the space in a specific moment (see table 2.3). Then, the solar

Inputs for the testing of NRLMSISE00 linearity	
Altitude	416000 [m]
Latitude	45°
Longitude	98°
Year	2018
Day of the Year	01/05/2018
UT seconds	0
Anomalous Oxygen flag	On

Table 2.3. Inputs for the testing of the linearity/non-linearity of the Thermosphere model NRLMSISE00

and geomagnetic indices have been varying through vectors of 100 linearly equally spaced points in MATLAB between the upper and the lower boundaries given by *Prophet*. Finally, the TMD has been evaluated with NRLMSISE00 model for every sample and the results confirmed the linear trend of TMD by varying the solar and geomagnetic indices (see figure 2.17). In order to double-check the results, another test has been performed changing the day (01/01/2020) and the altitude (302000 [m]) but the same results were achieved (see figure 2.18). This allowed to remove

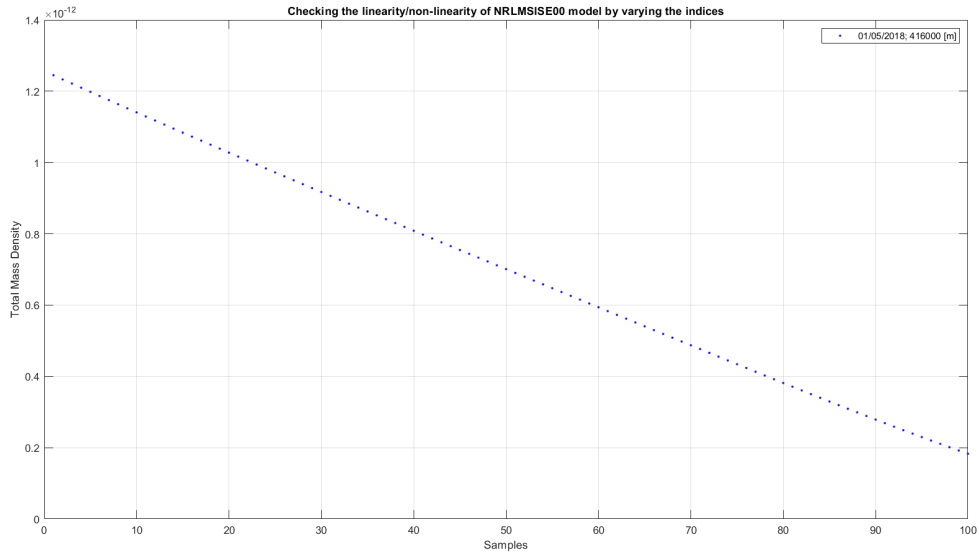


Figure 2.17. Testing linearity of NRLMSISE00 on 01/05/2018 at 416000 [m] of altitude

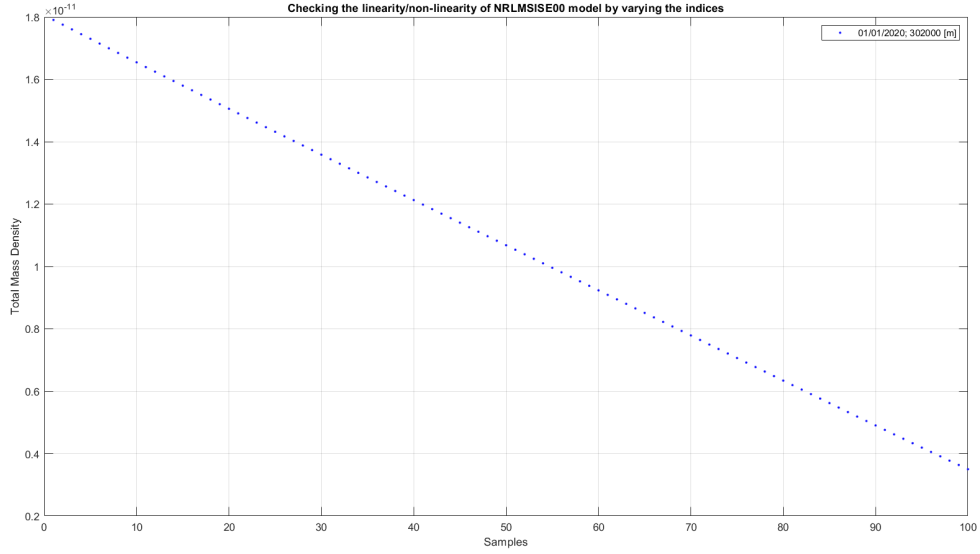


Figure 2.18. Testing linearity of NRLMSISE00 on 01/01/2020 at 302000 [m] of altitude

the optimizer from the model saving relevant computational times. The maximum and the minimum of TMD can be calculated just using the upper and lower values

given by *Prophet* (*'yhat_upper'* and *'yhat_lower'*) because they are already the values at the boundaries of the prediction of the indices and respectively of the TMD. Running one of the simulations which will be explained and described in chapter 4 about the calculation of the minimum re-entry time for a space object with area to mass ratio of $10 \frac{m^2}{kg}$ on 01/05/2018 with and without the optimizer, it is possible to observe the variation of the computational times (see table 2.4). This simulation is one of the fastest simulations which will be performed in the following chapters but the difference due to the absence of the optimizer is already clear and consistent, while the results are perfectly the same: 0.4995 days of minimum re-entry time.

Computational times	
With optimizer	720 [s]
Without optimizer	489 [s]

Table 2.4. Computational times for the minimum re-entry time of a $10 \frac{m^2}{kg}$ space debris on 01/05/2018

2.3.2 Orbit Propagator

Firstly, for the sake of convenience three models have been created: one for the maximum re-entry time calculation, one for the minimum re-entry time and the last one for the average times. They are identical and the only difference lies in the final value of TMD because the steps to calculate the TMD are pretty the same as it is reported above.

The maximum (or minimum or average, it depends on the model which is running) TMD is calculated at every step of the propagator calling the Thermosphere model everytime. The orbit propagator is essentially an Ordinary Differential Equation (ODE) solver which integrates the motion equations from an initial State Vector through a 3DoF analysis neglecting the attitude since the aim of the thesis is to study the uncertainty on the re-entry time windows and not the aerodynamic stability and dynamics of the objects during the decay phase (a 6DoF would be computationally too expensive in this case and it is not required). In addition to the inputs for the Thermosphere model the orbit propagator requires the following parameters:

- It is necessary to specify the radius, the period and the gravitational parameter

μ of the reference planet, which is the Earth in this case ($R_{Earth} = 6371[km]$, $T_{Earth} = 86164.09[s]$, $\mu = 398600[\frac{km^3}{s^2}]$);

- The Drag coefficient which depends on the case as reported in section 1.2;
- The area to mass ratio $\frac{S}{m}$ which gives information about the reference area and its mass;
- The orbital parameters of the orbit without perturbations:
 - The eccentricity e ;
 - The Right Ascension of the Ascending Node (RAAN) Ω ;
 - The argument of the Perigee ω ;
 - The inclination of the orbit i ;
 - The true anomaly ν ;
 - The semi-major axis a which can be derived from the previous parameters and the altitude specified before for the Thermosphere model:

$$a = \frac{(Altitude + R_{Earth})(1 + e \cos \nu)}{1 - e^2} \quad (2.1)$$

Since this is a 3DoF analysis the State Vector is composed of the three components of the radius vector and the 3 components of the velocity in the ECI coordinates. The initial value can be calculated from the orbital parameters through the following steps:

- From the trajectory equation (obtained with geometrical reasoning) the norm of the radius is known:

$$R = \frac{a(1 - e^2)}{1 + e \cos \nu} \quad (2.2)$$

- Then, comparing the trajectory equation from geometrical reasoning with the trajectory equation from energetic reasoning $R = \frac{h^2}{\mu(1 + e \cos \nu)}$ it is possible to calculate the moment of momentum:

$$h = \sqrt{a(1 - e^2)\mu} \quad (2.3)$$

- Considering the orbital plane of the object as illustrated in the figure 2.19 with the center in the center of the main body and the axis \vec{p} in the direction of the perigee, \vec{q} perpendicular to it on the orbital plane and \vec{w} perpendicular to the orbital plane, the coordinates of the radius vector and the velocity are known and they can be written as:

$$\begin{cases} R_p = R \cos \nu; \\ R_q = R \sin \nu; \\ R_w = 0; \end{cases} \quad \begin{cases} V_p = -\frac{\mu}{h} \sin \nu; \\ V_q = \frac{\mu}{h} \cos \nu; \\ V_w = 0; \end{cases}$$

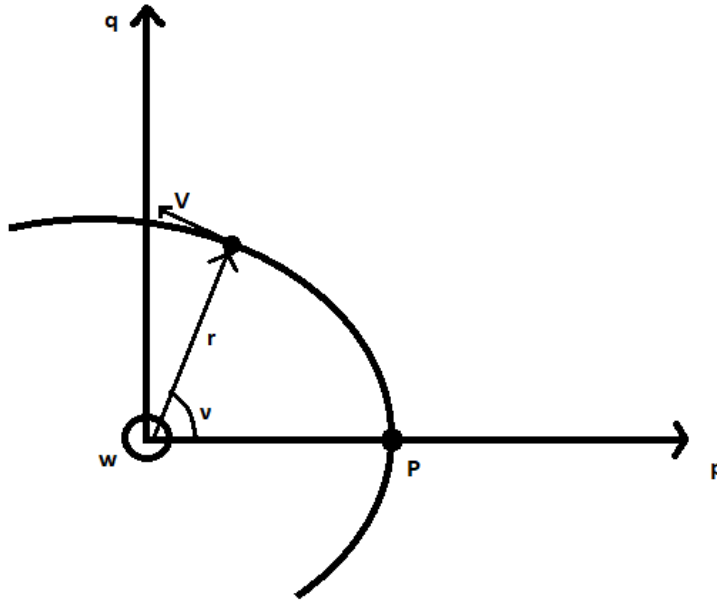


Figure 2.19. Orbital plane reference frame

- The State Vector shall be written in ECI reference frame (centered in the center of the main body with the equatorial plane as fundamental plane, the i axis in the direction of the vernal equinox, the k axis is in the direction of the Celestial North Pole and the j axis is perpendicular to both of them as it is illustrated in figure 2.20) in order to propagate a realistic orbit, hence a transformation of the reference frame is necessary and it is performed with the following rotational matrices which are called Transformation of Euler:

$$L_\Omega = \begin{bmatrix} \cos \Omega & \sin \Omega & 0 \\ -\sin \Omega & \cos \Omega & 0 \\ 0 & 0 & 1 \end{bmatrix} \quad L_i = \begin{bmatrix} 1 & 0 & 0 \\ 0 & \cos i & \sin i \\ 0 & -\sin i & \cos i \end{bmatrix} \quad L_\omega = \begin{bmatrix} \cos \omega & \sin \omega & 0 \\ -\sin \omega & \cos \omega & 0 \\ 0 & 0 & 1 \end{bmatrix}$$

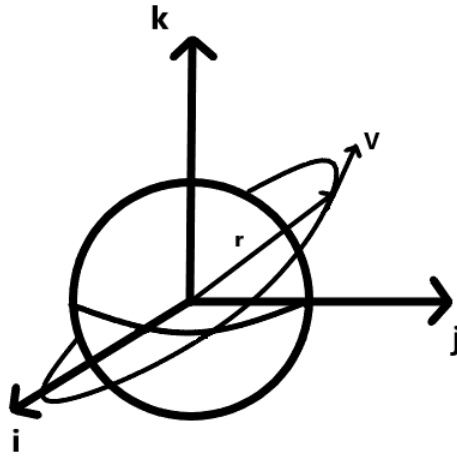


Figure 2.20. ECI reference frame

In order to transform the coordinates of a generic vector \vec{S} from the orbital plane reference frame to the ECI reference frame the right sequence is:

$$S_{ECI}^{\vec{}} = L_\Omega^T L_i^T L_\omega^T S_{PQW}^{\vec{}}$$

The initial State Vector is the initial point of the integration and it identifies a precise point in the orbit in a determined time. The integration is performed with one of the ODE solvers available in MATLAB: *ode113*. It integrates the system of differential equation which describes the motion of the object around the Earth from an initial time t_0 to the final time t_f specified in the inputs. This is a variable-step, variable-order (VSVO) Adams-Bashforth-Moulton PECE solver of orders 1 to 13. The highest order used appears to be 12, however, a formula of order 13 is used to

form the error estimate and the function does local extrapolation to advance the integration at order 13³. Compared to *ode45* (another broadly used ODE solver), it is more efficient with stringent tolerances and for this reason it is usually adopted for this kind of study. In fact, the relative tolerance has been set to 10^{-7} while the absolute tolerance has been set to 10^{-8} trying to find the right balance between accuracy and computational times. Moreover, the solver checks at every time step if the object reaches the Altitude of End Orbit which typically is about 120 [km] of altitude [11] (when the break up occurs and it reenters in the low Atmosphere) and in that case, it stops the integration.

Generally, the motion equation in a two-body problem in Space Flight Mechanics without perturbation forces is given by:

$$\vec{r} = -\frac{\mu}{r^3}\vec{r} \quad (2.4)$$

In this analysis, the only perturbation force considered is the Aerodynamic Drag. Therefore, it is necessary just to add the components of the Drag's acceleration (specified in the equation (1.1)) to the components of the acceleration without perturbation obtaining in this way:

$$\vec{r} = -\frac{\mu}{r^3}\vec{r} + r_{DRAG}\vec{r} \quad (2.5)$$

The most important thing is that the components of the Drag acceleration shall be always opposite to the components to the velocity, because by definition the Drag is the force that acts in the same direction of the velocity but in the opposite way. Finally, it is possible to identify the system which describes the motion of the object under the influence of the aerodynamic Drag around the Earth:

$$\text{Sys} = \begin{pmatrix} \dot{r}(1) \\ \dot{r}(2) \\ \dot{r}(3) \\ -\frac{\mu}{r^3}r(1) \pm \frac{1}{2}\rho\frac{C_{DS}}{m}\dot{r}^2(1) \\ -\frac{\mu}{r^3}r(2) \pm \frac{1}{2}\rho\frac{C_{DS}}{m}\dot{r}^2(2) \\ -\frac{\mu}{r^3}r(3) \pm \frac{1}{2}\rho\frac{C_{DS}}{m}\dot{r}^2(3) \end{pmatrix}$$

³See <https://www.mathworks.com/help/matlab/ref/ode113.html>

This is the system of the equations to be integrated to achieve the State Vector at every time step. This is the derivative of the State Vector and it is composed of the three components of the velocity before the integration (they are the boundary conditions) and of the three components of the acceleration at the same point.

The derivative of the State Vector is achieved at every time step through some points:

- First of all, Altitude, UTseconds, Date, Latitude and Longitude are updated during the propagation at every time step:
 - Altitude is simply updated subtracting the Earth radius to the norm of the first three components of the state vector used as the initial value of the new time step;
 - The UTseconds are updated with the length of the time step and they reset every time that they pass the 86400 [s] (1 day), updating, in this case, the Date, too;
 - The Latitude and the Longitude are updated using the Celestial Equatorial Coordinates *declination* δ and *Right Ascension* α (figure 2.21). Longitude is the angle measured from the Greenwich Meridian to the Meridian correspondent to the location of the space object. On the other hand, the Latitude is measured from the Equatorial plane to the Parallel which identifies the desired point. In the Celestial Equatorial coordinates they are described by the following laws during the space object motion and the rotation of the Earth:

$$\begin{cases} Lat = \delta; \\ Lon = \alpha - (\alpha_g + \omega_{Earth} T_{Earth}); \end{cases}$$

α_g identifies the Greenwich Meridian, while ω_{Terra} is referring to the rotation speed of the Earth. They are necessary in order to calculate the Longitude of the space object during the propagation of the orbit because the Earth is also rotating and it is essential to know the position of the Greenwich Meridian. This one can be calculated from the Date through the Julian Day (which is a continuous count of days with integer values) using the JD2000 as reference value and the empirical law of

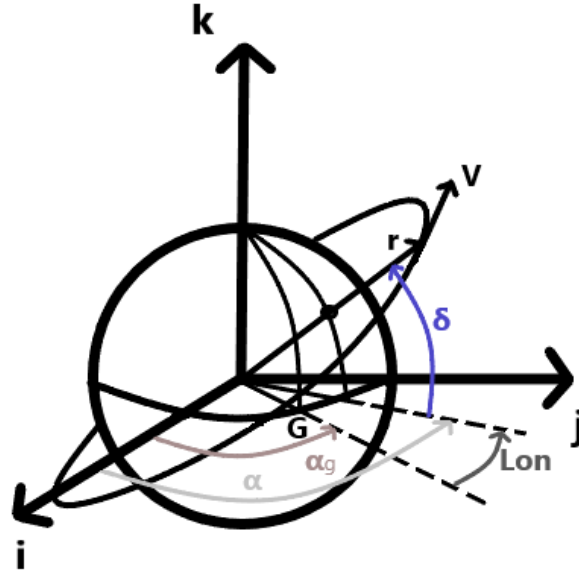


Figure 2.21. Celestial Equatorial coordinates

NASA:

$$\alpha_g = 280.45061837 + 360.98564736629 d + 0.0003875 T^2 \quad (2.6)$$

Where $d = JD - JD2000$ and $T = \frac{d}{36525}$. Once the value of α_g is known, it is possible to calculate the Latitude and the Longitude at every time step with the components of the radius vector in ECI coordinates and geometrical reasoning:

$$\begin{cases} \delta = \arcsin \frac{R_{ECI(3)}}{R_{ECI}}; \\ \alpha = \arctan \frac{R_{ECI(2)}}{R_{ECI(1)}}; \end{cases}$$

By this way, the Thermosphere model can calculate the TMD considering the geographical variations in the distribution of ρ itself, too;

- The solar and geomagnetic indices are updated from the catalogues created with *Prophet* by varying Date and UTseconds;
- The Thermosphere Model is called for the maximum (or the minimum) TMD for every single time step and thus for every single position of the space object during the orbit;
- Therefore, the components of the Drag's acceleration (checking that they are opposite to the velocity's components) are calculated through (1.1) achieving always the maximum (or the minimum) perturbation force and finally the derivative of the State Vector obtained through (2.5) is integrated by *ode113*;

When the integration stops because the altitude of end orbit has been reached, the re-entry time is the time spent by the solver for the integration of the equations.

Chapter 3

Validation Phase

To use the model described in the previous chapter for practical uses, it is necessary to validate it with a well-known case. As it is reported in the Literature one of the most famous re-entry campaign has been the one focused on The Gravity Field and Steady-State Ocean Circulation Explorer (GOCE). ESA proposed to analyse this spacecraft's re-entry for the IADC test campaign in 2013 trying to achieve important information about the structure of the Thermosphere and the forces which are present during the re-entry [14]. In fact, most of the payloads of GOCE remained on in measurement mode until the very end of the mission and this helped the scientific community to collect an important and broad amount of data, allowing GOCE to be considered a kind of a milestone for re-entry purposes.

3.1 GOCE re-entry modelling

For the reasons reported above, GOCE has been selected as the best test case for this work. The large amount of data achieved in 2013 has been made available to the public and this was very important for the following studies because it allowed getting a full data set about the re-entry phase ¹ ².

Before the re-entry phase began, GOCE was in a circular sun-synchronous orbit with

¹See <http://eo-virtual-archive1.esa.int/Index.html>

²See <https://earth.esa.int/web/guest/missions/esa-operational-eo-missions/goce/re-entry-special-dataset>

an in inclination of 96.71° and a RAAN of 90° . For circular orbits, the argument of perigee ω and the true anomaly ν are typically set to 0, because they are not well defined since every point could be the perigee. It was launched in 2009 from Plesetsk (Russia) and it operated for more than 4 years. It ran out of Ion Thrusters' propellant on 21 October 2013 at 03:16 UTC while it was at an altitude of 229 [km] as it was planned. During the re-entry the attitude control system was working and it maintained the spacecraft with head-on, minimum drag configuration keeping a coefficient of Drag C_D of around 3.5 until almost the very final phase [12] [14]. The spacecraft body had the shape of an octagonal prism with about 5.3 [m] of length and a transversal cross-section of about 1.1 [m^2] (see figure 3.1) while the weight is about 1100 [kg]. Since it was maintained with head-on configuration the reference area to consider is the transversal cross-section. According to the official reports,

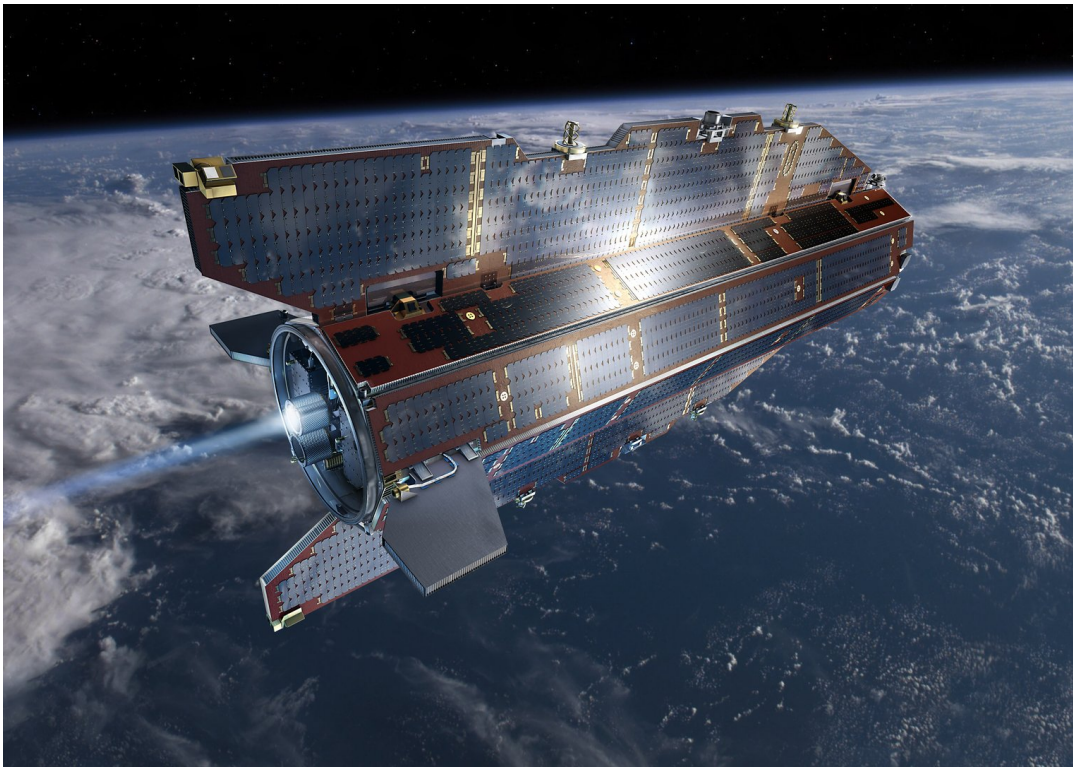


Figure 3.1. http://www.esa.int/ESA_Multimedia/Images/2009/05/GOCE_in_orbit

GOCE re-entered at the break-up altitude of 115 km on 11 November 2013 at 00:16 UTC. This data has been used as input in the simulations for the validation of the model and it is summarised in table 3.1.

GOCE Data set at the beginning of the re-entry phase	
Ion Thrusters off	21 October 2013 @ 03:16 UTC
Altitude	229000 [m]
Eccentricity	0
Inclination	96.7°
ν	0°
ω	0°
RAAN	90°
Mass	1100 [kg]
Reference Surface	1.1[m ²]
C_D	3.5

Table 3.1. GOCE Data Set used in the simulations for the validation of the model

3.1.1 Prediction of solar and geomagnetic indices for GOCE

Once the data about GOCE re-entry was collected, a prediction of the solar and geomagnetic indices has been made for the years interested by the GOCE re-entry, i.e. for 2013 and 2014 (just to be sure to have enough data). The prediction has been made with the same settings described in tables 2.1 and 2.2. By this way, the model for the validation is completely equivalent to the model described in the chapter 2. In fact, the real values of the indices were available in the catalogues of NOAA website but in order to have a re-entry time window the indices had to be predicted. Moreover, this was useful to prove once again the reliability of the predictions made by Prophet. Obviously, the only difference by the predictions made in chapter 2 is that the period considered is different. However, the range of years is basically the same, e.g. taking into account the years from 1975 to the end of 2012 for $F_{10.7}$ while before the range was from 1980 to 30/04/2018 (an analog consideration can be made for the geomagnetic indices). The results were really good and they are shown from the figure 3.2 to the figure 3.6.

As it is possible to observe, the geomagnetic indices are always difficult to estimate because they are often very similar low values and only sometimes there are peaks due to geomagnetic storms. However, they are not following any cycle and for this reason, the peaks are neglected. On the other hand, the prediction of the solar index $F_{10.7}$ is worthy of consideration because as it is possible to see from the figure 3.2 the fitting is really good and the trend is clearly visible and reliable. In fact, since the

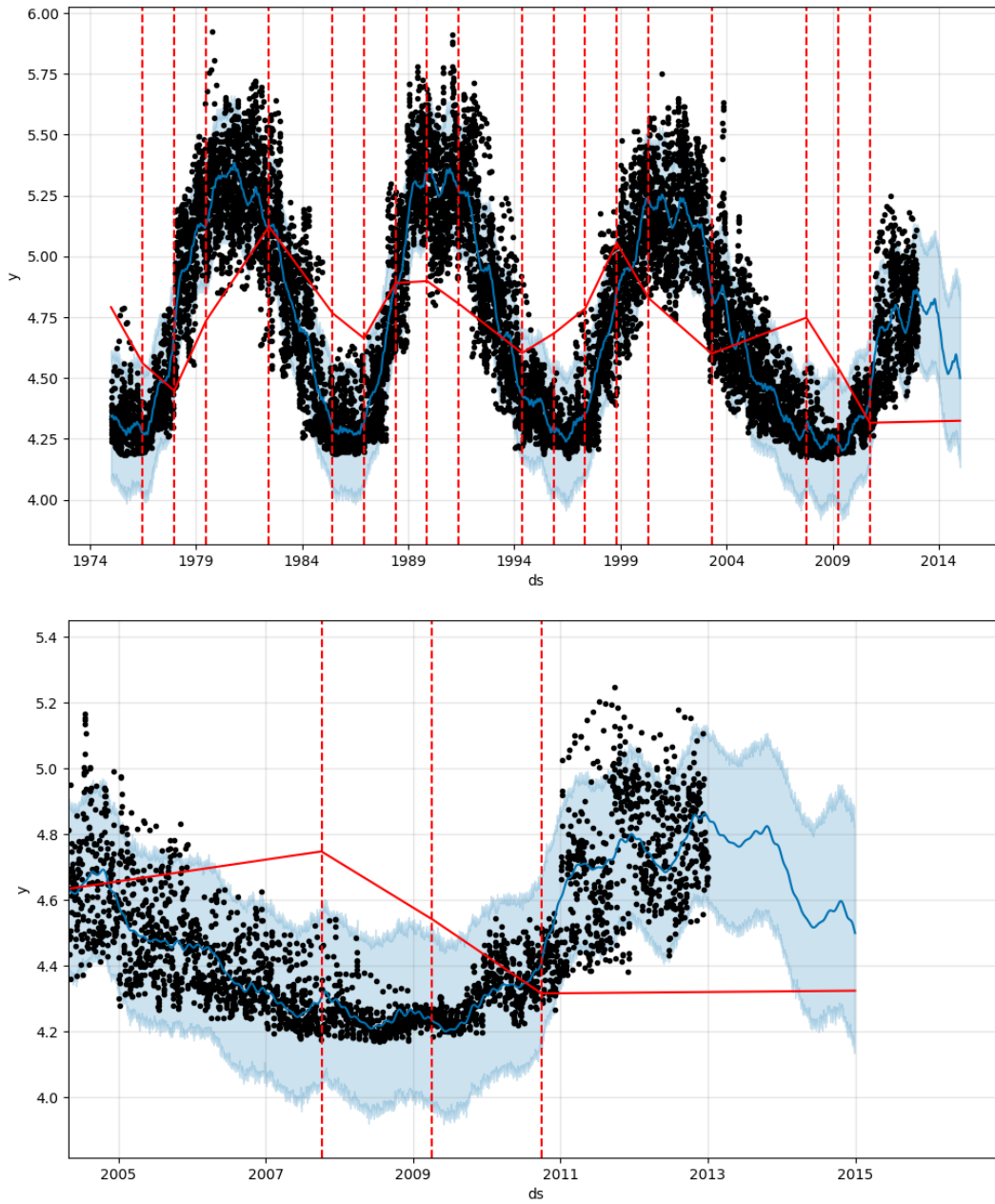


Figure 3.2. Prediction of $F_{10.7}$ solar index for 2013 and 2014 (above) and corresponding particular of the predicted values (below)

real data is available it is possible to compare the above mentioned prediction with the real values of the $F_{10.7}$ index during 2013 and 2014, as it is reported in figure 3.7. What emerges is that the forecasting model worked very well because most of

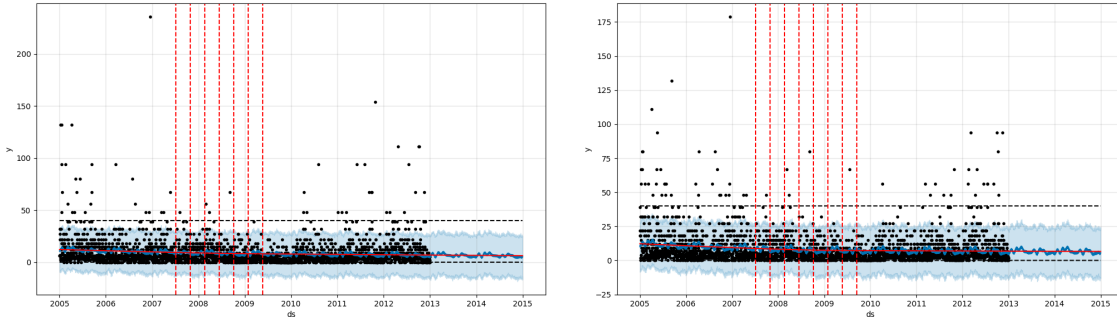


Figure 3.3. Prediction of a_{p0-3} (left) and a_{p3-6} (right) geomagnetic index for 2013 and 2014

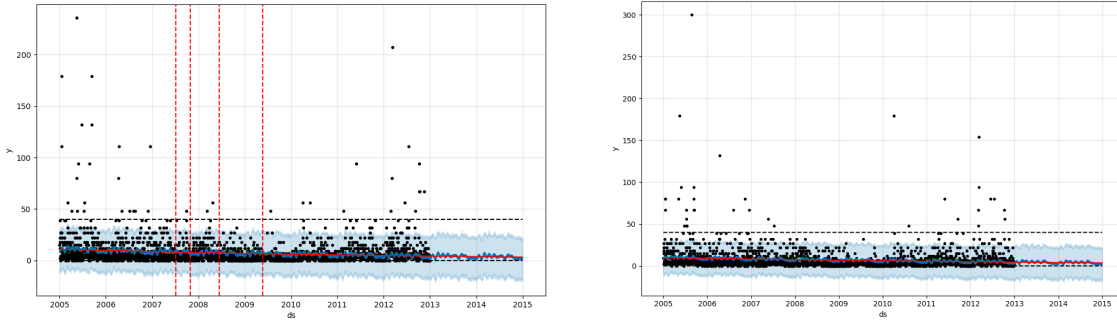


Figure 3.4. Prediction of a_{p6-9} (left) and a_{p9-12} (right) geomagnetic index for 2013 and 2014

the real values are included in the range given by *Prophet*, that is, especially for the prediction of 2013 (figure 3.8), between about 4.5 and 5 in the natural logarithmic scale (corresponding to about 90 [sfu] and 150 [sfu]). However, even here the peaks are unpredictable because they depend on the strength of the solar activity which is not always regular and this is the reason why some of the values are outside the estimation range. Moreover, the prediction of the indices seems to be getting worse while the period to predict increases. In fact, the prediction of 2014 values is still good but there are more values that are not included inside the light blue interval. Most of them are higher than the upper limit of the interval and this is attributable to the peaks above mentioned and therefore to the same problems related to them.

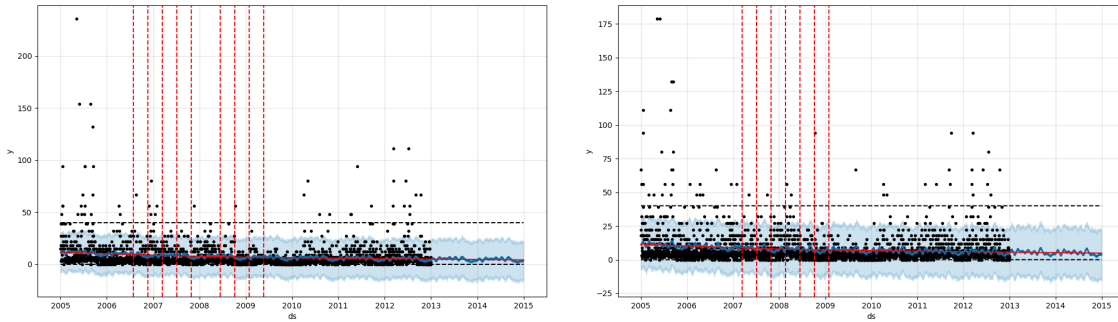


Figure 3.5. Prediction of a_{p12-15} (left) and a_{p15-18} (right) geomagnetic index for 2013 and 2014

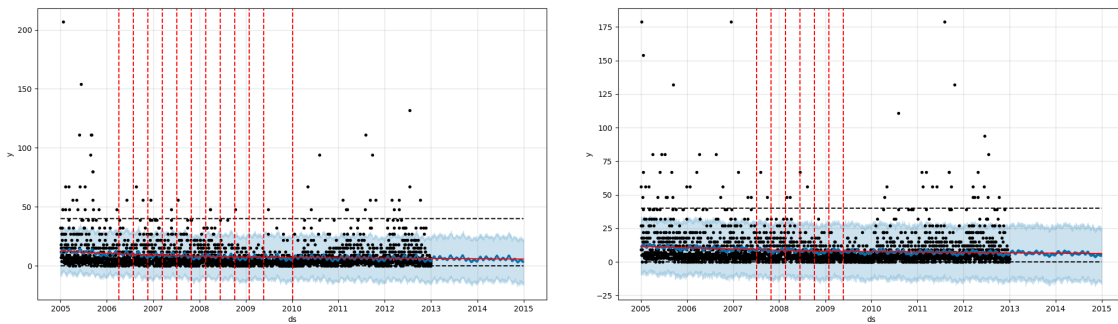


Figure 3.6. Prediction of a_{p18-21} (left) and a_{p21-24} (right) geomagnetic index for 2013 and 2014

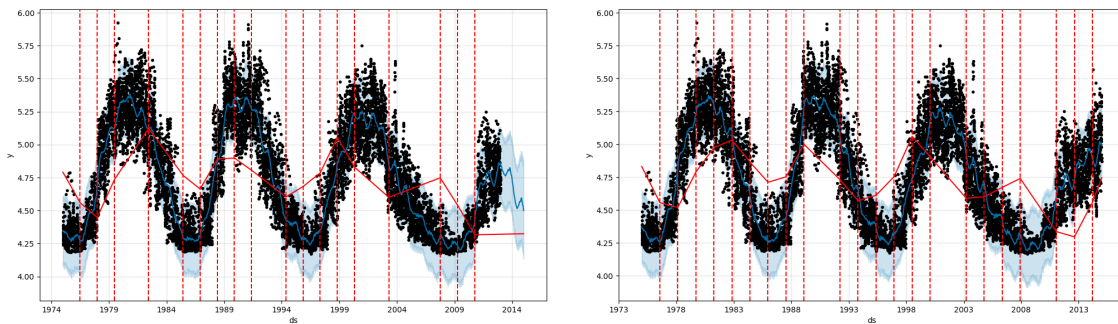


Figure 3.7. Comparison between predicted (left) and real (right) values of $F_{10.7}$ in 2013 and 2014

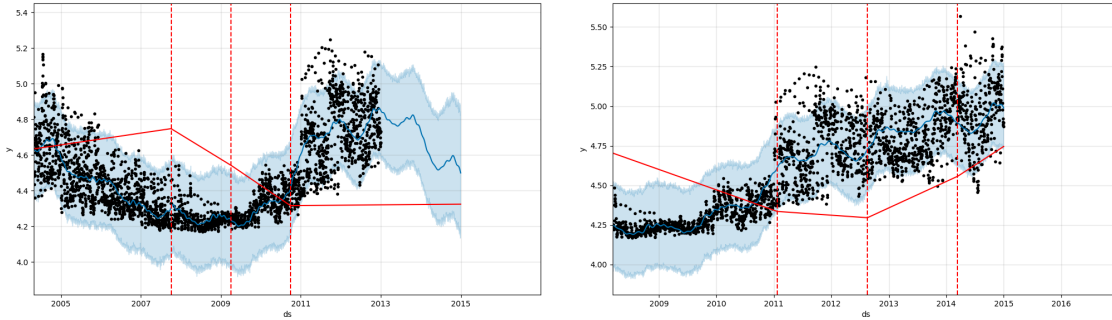


Figure 3.8. Details from figures 3.7 of the considered years, with on the left the predicted values and on the right the real ones

3.2 GOCE simulations

The simulations have been prepared with the inputs and the catalogues specified in the previous sections and the results have been carried out through the HPC cluster of *Strathclyde* due to the high computational times required for this kind of problem. In fact, the GOCE’s area to mass ratio is really low, therefore the re-entry times and the computational times are very high. Obviously, the simulations adopted the same model described in chapter 2, hence the orbit propagator uses a 3DoF approximation. This approximation didn’t influence the results because the attitude remained pretty constant during the re-entry and as it is illustrated in [8], the adoption of a 6DoF propagator would have been almost useless considering the much higher computational times required. Indeed, the 6DoF analysis doesn’t include a controlled attitude and in the numerical simulations reported in the same paper above mentioned GOCE remains aerodynamically unstable. For this reason, a 3DoF analysis is reliable even if the object has a complicated shape.

GOCE spent 21 days for the re-entry at the orbit of 115 [km], therefore the objective of the simulations was to achieve a reliable re-entry time window centered in the real date of re-entry. Two simulations have been performed: one looking for the maximum re-entry time using the minimum of the TMD and the other one looking for the minimum re-entry time using the maximum of the TMD. The results are reported in table 3.2, where it is clearly noticeable that the model is reliable and the prediction of the re-entry time is enough accurate.

The maximum re-entry time has a relative error on the real value of the re-entry

GOCE simulations results	
T_{MAX}	25.4 Days
T_{MIN}	15.13 Days

Table 3.2. The re-entry time window for GOCE

time of:

$$\frac{25.4 - 21}{21} = +21\%$$

while the minimum re-entry time has an error of:

$$\frac{15.13 - 21}{21} = -27\%$$

with the same confidence interval (90%, see section 2.2) which has been set in the properties of *Prophet* predicting the indices. It is also important to specify that the prediction of $F_{10.7}$ and a_p has been made from the beginning of 2013, therefore the values used as input in the Thermosphere model are already values predicted 10 months before and for this reason the uncertainty included can be higher than in simulations with real values of the indices until the day before the simulation itself. It has been decided to have a prediction of 10 previous months in order to simulate the most general case possible.

An important feature to show is the behaviour of the altitude during the re-entry for both the simulations performed and the the real values of GOCE ³. In the figure 3.9, the altitude range of GOCE using the values of the altitude of every date of the re-entry at 00:00 UTC is reported for all the three cases. The real values of the altitude are always included inside the re-entry time window created by the maximum and minimum re-entry time curves. The orbit during the Decay Phase doesn't have huge variations other than the altitude. The decay is quite regular and it becomes faster in the last couple of days, below an altitude of about 185 [km] where the value of the drag increases since the TMD grows. A qualitative representation of the decay phase is reported in figure 3.10 and 3.11 about the maximum re-entry time decay. The results are fulfilling and the reliability of the model has been verified with the GOCE test case, where the uncertainty on the predicted solar and

³Real values of GOCE re-entry are available on ESA website http://eo-virtual-archive1.esa.int/products/DE_ORBITING/GOCE_QC_RPT_Deorbiting_1.0.pdf

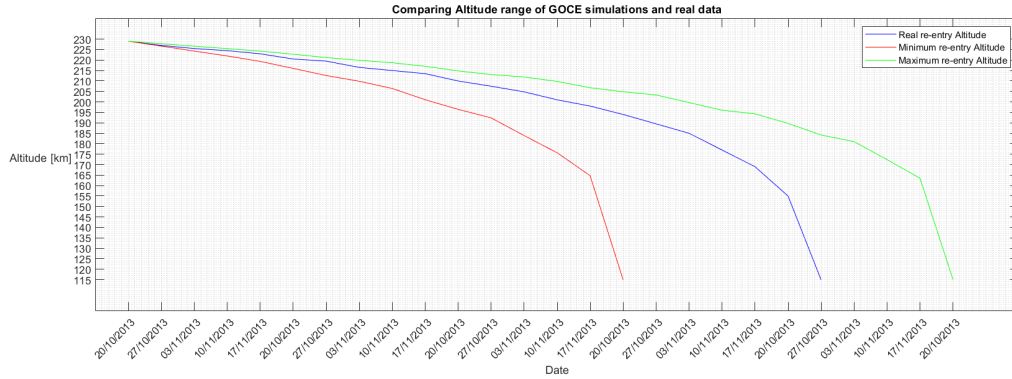


Figure 3.9. Altitude range comparison for the re-entry time window of GOCE

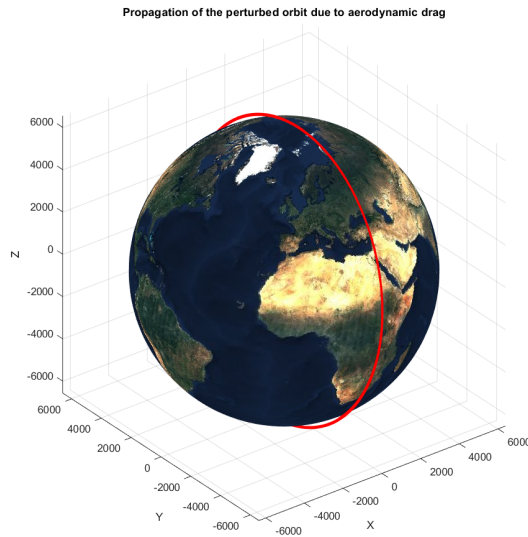


Figure 3.10. GOCE's orbit decay

geomagnetic indices leads to an uncertainty on the re-entry time which is acceptable and comparable to the typical uncertainties available in Literature.

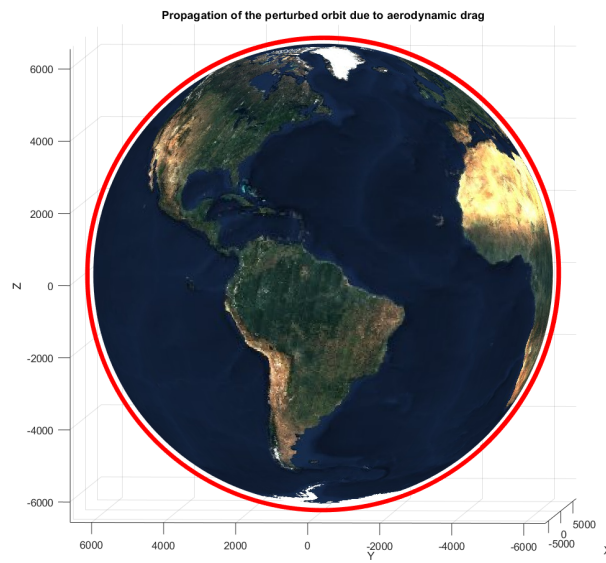


Figure 3.11. Top view of GOCE's orbit decay

Chapter 4

Analysis of a practical application

The validation has demonstrated the goodness of the model, while here the objective is to show its potential analysing well defined practical cases. Firstly, dealing with orbits under 1000 [km] of altitude in LEO, the model has no restrictions about the initial orbit properties or about the properties of the object, but it has just to comply with some conditions:

- The orbital parameters of the initial orbit or the initial state vector must be known;
- The reference surface area of the object and its mass must be known;
- The model depends just on the limits of the Thermosphere model, e.g. the altitude of the orbit shall always be below 1000 [km] during the propagation, in order to remain inside the Thermosphere boundaries and calculate TMD;

The possible applications are very extensive but in this work the focus will be on the analysis of the decay phase of an interesting class of space objects: the high area to mass ratio group. This one will be introduced in section 4.1.

For this analysis, the reference initial orbit has been identified in the ISS orbit, and in particular, the orbital parameters from the TLE¹ of ISS on 11/02/2020 at 00:00 UTC have been used as initial conditions:

```
1 25544U 98067A 20042.00489325 .00016717 00000 - 0 10270 - 3 0 9073
```

¹From <https://heavens-above.com/orbit.aspx?satid=25544> website, where TLE of ISS passes are reported daily

2 25544 51.6402 257.7596 0005085 255.3043 104.7544 15.49127287 12296

Basically, the ISS orbit has been selected because its data availability is in the public domain, it is reliable data and the simulations can start from a moderate altitude allowing to further reduce the computational times. Another reason is that, eventually, several ISS elements can be considered as high area to mass debris (like solar panels or thermal blankets) in the unlucky case of a collision or for a particular disposal plane. Thus, these simulations could be useful also for real practical application.

4.1 High area to mass ratio space objects

This particular class of space objects can include elements of satellites as for example solar panels or thermal blankets already cited for the ISS case or it can consider even particular passive devices for re-entry purposes which are called Drag Sails. Basically, these ones are quite new ideas of drag augmentation systems and they can be applied to small debris or space objects (for example nano-satellites) in order to increase the drag efficiency and reduce the re-entry times. They are still under-studies for problems related for example to the attitude and to the aerodynamic stability (a 6DoF would be more useful in this case) during the re-entry phase but they are an interesting solution that will be deepened in the next years according to the literature. An overview is given in [11], where an accurate analysis based on how the re-entry time of high area to mass ratio debris and objects equipped with drag sails (including a focus on the aerodynamic stability) varies with the orbital parameters, the area to mass ratio, the shape of the objects and the attitude (for non-spherical debris). In these simulations, it has been used a *Jacchia-Gill* Thermosphere model but the parameters relative to the solar and geomagnetic indices were held constants during the propagation with monthly average values. Then, the reasons for the choice of this class of space objects in the following simulations presented in section 4.2 can be summarised in:

- The will to add detail to the studies began in [11] from the *University of Strathclyde* and *Belstead* research group, analysing how the uncertainty on the prediction of the solar and geomagnetic indices can influence the estimation of the re-entry time window in this kind of problems;

- This class of space objects reduces considerably the computational times of the simulations (they are already high because the orbit propagator calls the Thermosphere model and update the inputs from the catalogues at every step) due to the higher value of area to mass ratio which involves a higher drag and a reduced re-entry time, hence it is not necessary the use of the HPC cluster used for the GOCE test case;

In this work, the focus will be more on the space debris than on drag sails, because the latter would require a higher fidelity propagator with a 6DoF analysis. The space debris analysed in [11] have a range of area to mass ratio from 1 [$\frac{m^2}{kg}$] to 10 [$\frac{m^2}{kg}$], hence the same range has been considered.

4.2 Simulations and results

Essentially, twenty-seven simulations have been prepared in order to study the influence of the uncertainty of the solar and geomagnetic indices on the re-entry times of high area to mass ratio space debris and they are summarised in table 4.1 and explained below.

As it has been anticipated in section 2.2, it is difficult to find a trend in the geomag-

Summary of the planned simulations with the key parameters									
Initial Date	1 [$\frac{m^2}{kg}$]			5 [$\frac{m^2}{kg}$]			10 [$\frac{m^2}{kg}$]		
01/05/2018	T_{MAX}	T_{MIN}	T_{AVG}	T_{MAX}	T_{MIN}	T_{AVG}	T_{MAX}	T_{MIN}	T_{AVG}
01/01/2020	T_{MAX}	T_{MIN}	T_{AVG}	T_{MAX}	T_{MIN}	T_{AVG}	T_{MAX}	T_{MIN}	T_{AVG}
01/01/2021	T_{MAX}	T_{MIN}	T_{AVG}	T_{MAX}	T_{MIN}	T_{AVG}	T_{MAX}	T_{MIN}	T_{AVG}

Table 4.1. Planned simulations for high area to mass ratio space debris

netic indices prediction, then it is difficult to find the periods when the geomagnetic activity is stronger. On the other hand, it is much easier to deal with solar index $F_{10.7}$ prediction because solar activity complies with the solar cycle which lasts about 11 years. For these reasons, it has been decided to simulate three periods with different intensity of the solar activity predicted in section 2.2 (see figure 4.1). In this way, it has been possible to analyse how the re-entry time window varies with both the intensity of the solar activity and the uncertainty which lies in its prediction.

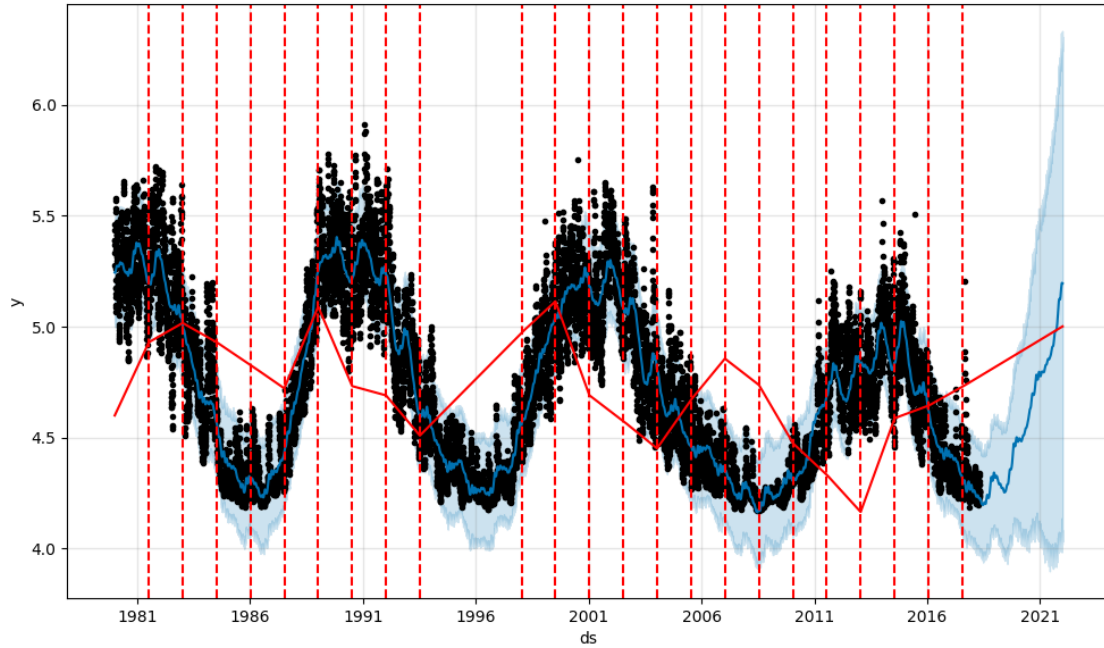


Figure 4.1. Prediction of solar index $F_{10.7}$ adopted in the simulations

In fact, the real data of the catalogues used for the predictions ends on 30/04/2018, while the initial day of the simulations are 01/05/2018 (low solar activity, 1 day after the last empirical value), 01/01/2020 (medium solar activity, 610 days after the last empirical value), 01/01/2021 (high solar activity, 976 days after the last empirical value). As it has been anticipated before and it is possible to observe in figure 4.1 with the light blue interval, the uncertainty included in the prediction of the indices increases as the period to forecast increases, hence, for example, it is expected that the simulations relative to the high solar activity should have a wider re-entry time window than the ones for the low solar activity. The objective of this work is to characterize the uncertainty present in this kind of problems, through the propagation of the uncertainty initially present in the solar and geomagnetic indices during the decay phase of a space object. In order to achieve a re-entry time windows at least two simulations for every case should be performed: the first one for the maximum re-entry time and the second one for the minimum re-entry time, because it is the difference between this two results. Since the re-entry time windows can be really wide, it has been useful to run another simulation about the average re-entry time for every case using the average values of the indices prediction given

by *Prophet*. However, it has been decided to run simulations only for area to mass ratio of 1, 5 and 10 [$\frac{m^2}{kg}$], trying to keep a reasonable number of cases and at the same time aiming to give an overview about how the area to mass ratio influences the re-entry time window.

The simulations contain the model described in chapter 2 but the initial conditions need to be specified. As mentioned before, the initial orbital conditions come from the TLE of ISS on 11/02/2020 at 00:00 UTC and they are resumed in table 4.2.

An important assumption has been made for these simulations: during the decay

Initial orbital conditions for simulations of high area to mass debris	
Altitude	416000 [m]
Eccentricity	0
Inclination	51.64°
ν	0°
ω	255.3°
RAAN	257.76°

Table 4.2. Initial orbital conditions corresponding to TLE of ISS orbit on 11/02/2020 at 00:00 UTC used in the simulations

phase the object is randomly tumbling. Through this hypothesis, it is possible to adopt the 3DoF propagator explained in section 2.3 because it allows to approximate the shape of the space object as a sphere since the attitude and the lift are neglected. Moreover, the modeling of the space object as a sphere helps in the choice of the C_D . The classical range of values for spherical space objects in LEO vary from 2.2 to 2.4 [2] (see section 1.2), hence in this work, a C_D of 2.3 has been considered since the studied debris are not real objects orbiting around the Earth (there is not an empirical value as for example there was with the GOCE case) and for this reason, a mean value is required. The simulations stop when the typical altitude of end orbit is reached, which in these cases is usually about 120 [km].

The simulations are based on the prediction of the solar and geomagnetic indices showed in section 2.2, hence they are available from 01/05/2018 until 20/11/2021. In fact, even if the predictions made are until the 31/12/2021, the adopted Thermosphere model is NRLMSISE00 and it requires the 81-day average of $F_{10.7}$ centered in the day of the prediction, therefore the last day available for the simulations is the 20/11/2021 because the model needs the values of $F_{10.7}$ for the following 40 days,

too.

4.2.1 Low solar activity and low uncertainty results

The first set of simulations considers as starting date 01/05/2018, therefore it refers to the low solar activity period in figure 4.1. Moreover, this should correspond to one of the simulations with the lowest uncertainty, since the real data availability ends on 30/04/2018 and it's only been one day until the day of the prediction. In fact, as it is also possible to observe in the above mentioned figure, the uncertainty range seems to be one of the tightest. However, this is how typically it is expected to be, but the light blue interval shows some small oscillations in the prediction of the indices and this could cause changes to this behaviour as it is possible to observe in the simulations with medium uncertainty.

The results of this first set are presented in table 4.3 and they are consistent with the behaviours previously illustrated in this work. In fact, the simulations show the

Low solar activity: 01/05/2018				
Low uncertainty: 1 day after the last empirical value				
Area to mass ratio	Window	T_{AVG}	T_{MAX}	T_{MIN}
1 $[\frac{m^2}{kg}]$	16.69385 [dd]	9.34613 [dd]	21.61230 [dd]	4.91845 [dd]
5 $[\frac{m^2}{kg}]$	3.09881 [dd]	1.85062 [dd]	4.08751 [dd]	0.98870 [dd]
10 $[\frac{m^2}{kg}]$	1.54039 [dd]	0.93593 [dd]	2.03995 [dd]	0.49956 [dd]

Table 4.3. Results in days for low solar activity and low uncertainty simulations

expected results:

- the re-entry time windows decrease significantly as the area to mass ratio increase;
- by varying the area to mass ratio, the difference among maximum times are higher than the differences among minimum times;
- the average times are closer to the minimum re-entry times than to the maximum re-entry times;

Concerning the last point, it is possible to better observe this behaviour analysing the relative errors of the maximum and minimum re-entry time in relation to the

average ones (see table 4.4) through the following laws:

$$Err_{T_{MAX}} = \frac{T_{MAX} - T_{AVG}}{T_{AVG}}$$

$$Err_{T_{MIN}} = \frac{T_{MIN} - T_{AVG}}{T_{AVG}}$$

It is clear that the relative errors for the maximum re-entry times are much bigger

Low solar activity: relative errors		
Area to mass ratio	Relative error for T_{MAX}	Relative error for T_{MIN}
1 $[\frac{m^2}{kg}]$	131.24%	-47.37%
5 $[\frac{m^2}{kg}]$	120.87%	-46.57%
10 $[\frac{m^2}{kg}]$	117.96%	-46.62%

Table 4.4. Relative errors for low solar activity and low uncertainty simulations

than the ones for the minimum re-entry times. This is caused by the minimum values of the indices. In fact, they tend to include all the possible values keeping the lower boundary of the uncertainty interval really low since the confidence interval was set to 90%. During the time series analysis, it is believed that the software includes the possibility that the lower solar activity period could last more than the previous ones and it considers the values in the same band as possible values since the last real values were referring to the low solar activity period. Moreover, it is possible to observe that the errors are decreasing as the area to mass ratio is increasing due to the propagation times. These are decreasing as the area to mass ratio is increasing and for this reason, the error on the final re-entry time doesn't have enough physical time to grow.

Concerning the orbital motion during the decay phase, there are not particular variations in the orbital parameters, except the semi-major axis obviously. Observing the decay phase for different area to mass ratio, the only worthy aspect is that during the orbit propagation of space objects with a higher area to mass ratio, i.e. 10 $[\frac{m^2}{kg}]$, the initial circular orbit tends to become slightly elliptical. The ellipticity has not been measured but the orbit remains almost circular. In fact, it can just be noticed that the altitude globally decreases but in the spiral during the decay phase it has sections in each orbit where it increases by about 8/10 [km] (see figure 4.2). This aspect is not so evident with area to mass ratio of 1 $[\frac{m^2}{kg}]$ and the variation of

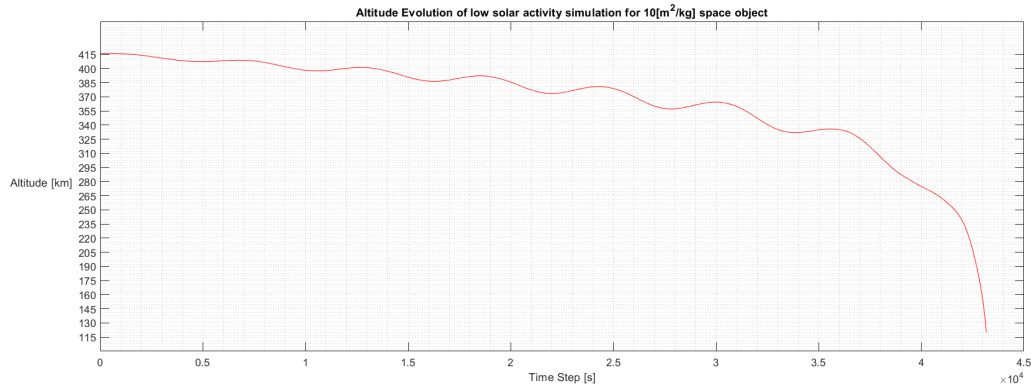


Figure 4.2. Altitude evolution during the decay phase for space object of $10 \left[\frac{m^2}{kg} \right]$ in low solar activity minimum re-entry time simulation

the altitude is almost negligible as it is reported in figure 4.3, which refers to the same simulation of the previous figure but for a space object of $1 \left[\frac{m^2}{kg} \right]$. The main reason is that with higher area to mass ratio the influence of the aerodynamic drag rises and the differences on the orbit properties are bigger. These characteristic are

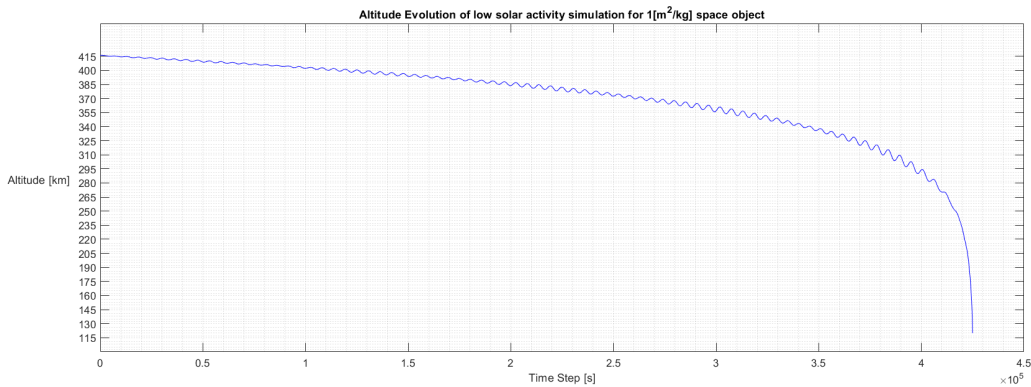


Figure 4.3. Altitude evolution during the decay phase for space object of $1 \left[\frac{m^2}{kg} \right]$ in low solar activity minimum re-entry time simulation

not visible from the qualitative representations of the orbit decay reported in figure 4.4 and 4.5, where it is only possible to observe that the orbits are more distinct and the decay phase is steeper for the space object with $10 \left[\frac{m^2}{kg} \right]$.

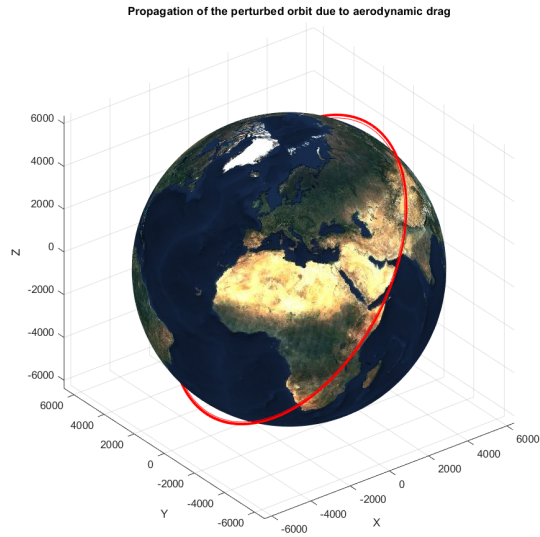


Figure 4.4. Orbit decay phase for space object of $10 \left[\frac{m^2}{kg} \right]$ in low solar activity minimum re-entry time simulation

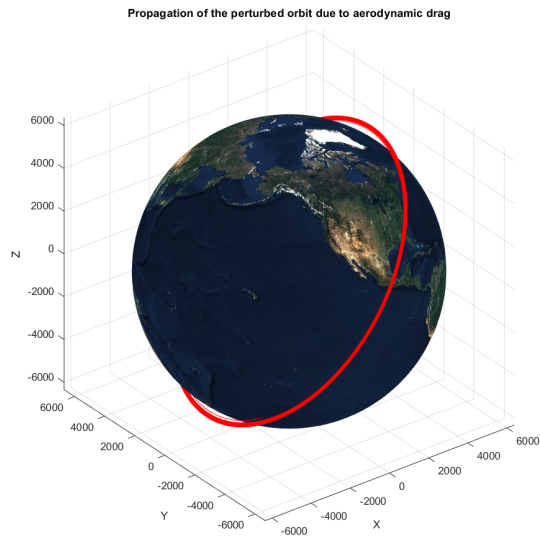


Figure 4.5. Orbit decay phase for space object of $1 \left[\frac{m^2}{kg} \right]$ in low solar activity minimum re-entry time simulation

4.2.2 Medium solar activity results

The second set of simulations considers the medium solar activity and consequently the medium uncertainty. The starting date of the simulations is 01/01/2020 (610 days after the last empirical value), but the other parameters are the same as the first set of simulation. The results are reported in table 4.5. As it has been anticipated

Medium solar activity: 01/01/2020				
Medium uncertainty: 650 days after the last empirical value				
Area to mass ratio	Window	T_{AVG}	T_{MAX}	T_{MIN}
1 [$\frac{m^2}{kg}$]	15.927663 [dd]	6.4667 [dd]	18.718163 [dd]	2.7905 [dd]
5 [$\frac{m^2}{kg}$]	3.0926 [dd]	1.2923 [dd]	3.659 [dd]	0.5664 [dd]
10 [$\frac{m^2}{kg}$]	1.5293 [dd]	0.6543 [dd]	1.8236 [dd]	0.2943 [dd]

Table 4.5. Results in days for medium solar activity and medium uncertainty simulations

before, comparing table 4.5 with table 4.3 it is possible to observe that the re-entry time windows for the medium uncertainty simulations are almost the same or less than the ones for the low uncertainty simulations due to the oscillation in the uncertainty interval of the predictions. The absolute values of average, maximum and minimum re-entry times for medium uncertainty case are lower than the low uncertainty ones and this was expected, too. In fact, the increased solar activity implies an increased TMD, an increased Drag and consequently a reduction in the re-entry times.

These results are highlighted by the values of the relative errors, which are reported in table 4.6. The relative errors for the maximum re-entry times show a consistent

Medium solar activity: relative errors		
Area to mass ratio	Relative error for T_{MAX}	Relative error for T_{MIN}
1 [$\frac{m^2}{kg}$]	189.45%	-56.85%
5 [$\frac{m^2}{kg}$]	183.14%	-56.17%
10 [$\frac{m^2}{kg}$]	178.71%	-55.02%

Table 4.6. Relative errors for medium solar activity and medium uncertainty simulations

growth compared to the low uncertainty simulations results and compared to the

relative errors for the minimum re-entry times, too. This means that the average re-entry times are still closer to the minimum re-entry time values than to the maximum ones, confirming the trend already explained for the low solar activity results. The orbital motion for this set of simulations shows the same properties already reported for the low solar activity results (see figure 4.6 and 4.7), but obviously, the re-entry times for these simulations are shorter and for this reason, the effects explained for the figure 4.2 are highlighted with higher solar activity because it implies higher values of TMD and consequently higher Drag. The variation of the

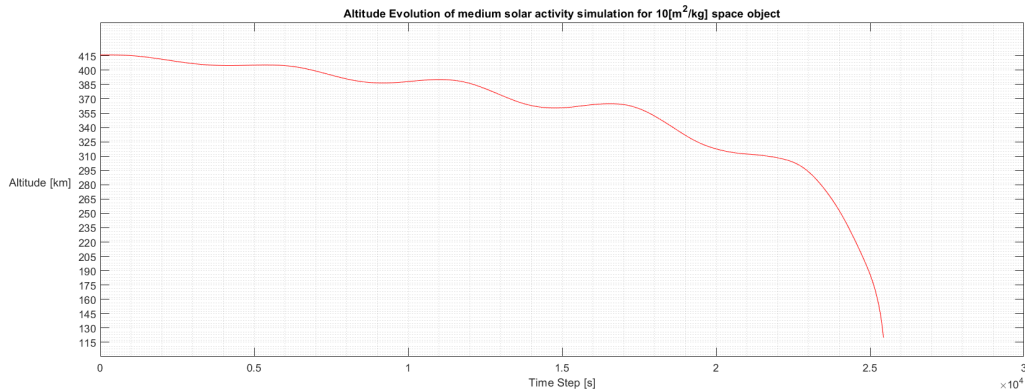


Figure 4.6. Altitude evolution during the decay phase for space object of $10 \left[\frac{m^2}{kg} \right]$ in medium solar activity minimum re-entry time simulation

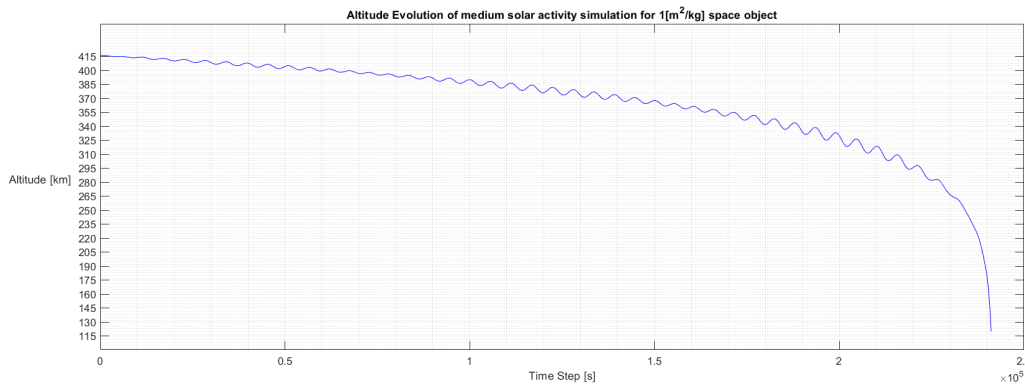


Figure 4.7. Altitude evolution during the decay phase for space object of $1 \left[\frac{m^2}{kg} \right]$ in medium solar activity minimum re-entry time simulation

altitude becomes consistent (until about 20/30 [km] difference on each orbit) for the

minimum re-entry time simulation of the decay phase for a space object of $10 \left[\frac{m^2}{kg} \right]$ and medium solar activity.

4.2.3 High solar activity results

The last set of simulations analyses the effects of the high solar activity and high uncertainty period. The only difference with the previous set of simulations is that the starting date is 01/01/2021 (976 days after the last empirical value). The results are reported in table 4.7. It is possible to note an increase in the values of the re-

High solar activity: 01/01/2021				
High uncertainty: 976 days after the last empirical value				
Area to mass ratio	Window	T_{AVG}	T_{MAX}	T_{MIN}
1 $\left[\frac{m^2}{kg} \right]$	17.426125 [dd]	3.6758 [dd]	18.51 [dd]	1.083875 [dd]
5 $\left[\frac{m^2}{kg} \right]$	3.3565 [dd]	0.7518 [dd]	3.5885 [dd]	0.232 [dd]
10 $\left[\frac{m^2}{kg} \right]$	1.6723 [dd]	0.3767 [dd]	1.798 [dd]	0.1257 [dd]

Table 4.7. Results in days for high solar activity and high uncertainty simulations

entry time window compared to the first two set of simulations and at the same time a decrease in the single values of average, maximum and minimum re-entry times. This behaviour is exactly what was expected and it agrees with what has been anticipated before. In fact, the uncertainty interval grows significantly as the starting date of the period to predict is further from the last empirical value. On the other hand, the high solar activity period implies lower values of the re-entry times for the usual consequences: higher solar activity, higher TMD, higher Drag and lower re-entry times.

The relative errors grow exponentially from the previous sets of simulations and they are reported in table 4.8. Especially, the relative errors for the maximum re-entry times are huge. As it is possible to note in figure 4.1, the uncertainty interval is really wide at the beginning of 2021, with the lower boundary still similar to the lower values of the first set of simulations and the reason has already been explained for the low solar activity results. Once again, the average values are closer to the minimum re-entry times, which maintain reasonable values of the relative errors even if the last empirical value is referring to 976 days before.

High solar activity: relative errors		
Area to mass ratio	Relative error for T_{MAX}	Relative error for T_{MIN}
1 $[\frac{m^2}{kg}]$	403.56%	-70.51%
5 $[\frac{m^2}{kg}]$	377.32%	-69.14%
10 $[\frac{m^2}{kg}]$	377.3%	-66.63%

Table 4.8. Relative errors for high solar activity and high uncertainty simulations

About the orbital parameters it is confirmed the trend showed in the previous sets. The variation of the altitude with the time step is reported for the two extreme cases of 1 $[\frac{m^2}{kg}]$ and 10 $[\frac{m^2}{kg}]$ space objects in figure 4.8 and 4.9. The only difference

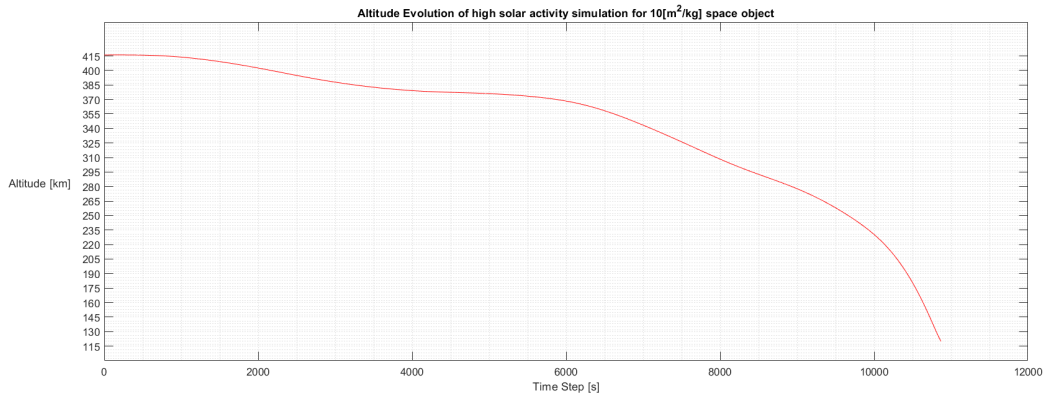


Figure 4.8. Altitude evolution during the decay phase for space object of 10 $[\frac{m^2}{kg}]$ in high solar activity minimum re-entry time simulation

with the previous sets is the starting date and in this case, it is possible to note that the oscillations become larger and lighter because the propagation times are shorter and the aerodynamic drag is higher.

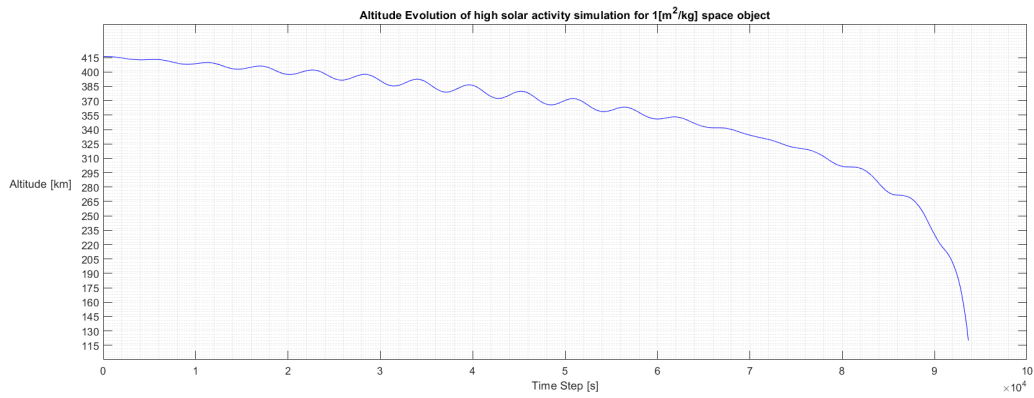


Figure 4.9. Altitude evolution during the decay phase for space object of $1 \left[\frac{m^2}{kg} \right]$ in high solar activity minimum re-entry time simulation

Chapter 5

Conclusions

The Thesis presents the model and the related results to characterize the uncertainty on the re-entry time of different space objects in LEO with the prediction of the solar and geomagnetic indices which influence the Total Mass Density (TMD) in the Thermosphere and consequently the atmospheric Drag. The model neglects the attitude of the space object and it shows only the limitations of the Thermosphere model (*atmosnrlmsise00*) which is implemented in the orbit propagator. The validation of the model has been carried out with the well-known test case of GOCE, achieving very accurate predictions.

The obtained results have pointed out an increase of the re-entry time windows as the starting date is far from the last predicted value with a consequential decrease in the single values for minimum, maximum and average re-entry time windows as the solar activity (here the different levels of activity are distinguished, unlike the geomagnetic activity) increases and in this case, the two effects are connected (see figure 5.1 for a summary graph). Moreover, analysing the results is possible to note that the average re-entry times are closer to the minimum re-entry times. In particular, the most reliable values of the re-entry times are between the minimum re-entry time value and the average one for simulations which use predictions of the solar and geomagnetic indices far from the last predicted value as it is possible to note analysing the relative errors (e.g. the third set of simulations). The reason lies in the prediction of solar indices. In fact, it is expected from the previous solar cycle an increase in the trend of solar index $F_{10.7}$ for the predicted years (2018-2021) but the confidence interval from the time series analysis achieved with *Prophet* tends to

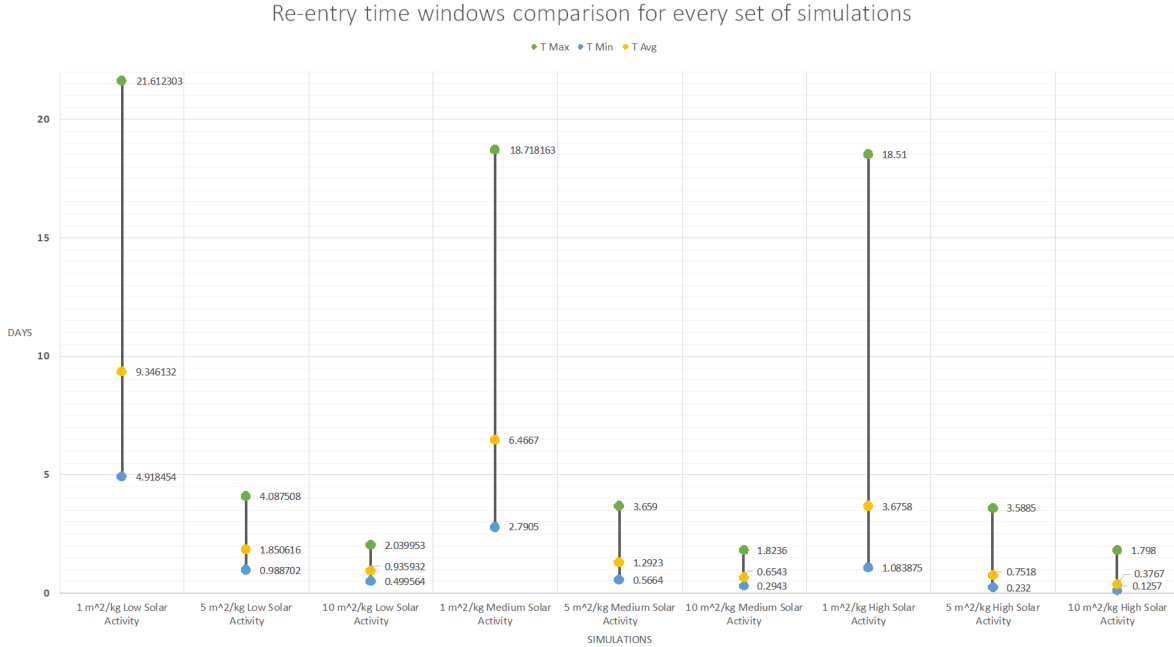


Figure 5.1. Re-entry time windows comparison for every set of simulations performed

include conservatively the possibility that lower values similar to the initial values exist. An approach to future more accurate results has been identified in a more accurate time series analysis. In fact, two of the simulations performed in chapter 4 (the simulations for T_{MAX} and T_{MIN} of a space object of $10 [\frac{m^2}{kg}]$ during low solar activity and low uncertainty period) have been tested with an artificial reduction of 20% on the upper values of the predicted solar and geomagnetic indices and an artificial increase of 20% on the lower boundaries. In this way, the uncertainty on these indices has been reduced and it has been verified a reduction of the re-entry time windows, too (see table 5.1). Comparing the results with the re-entry time

Artificial reduction of solar and geomagnetic activity uncertainty			
Area to mass ratio	Window	T_{MAX}	T_{MIN}
$10 [\frac{m^2}{kg}]$	0.66513 [dd]	1.421385 [dd]	0.756255 [dd]

Table 5.1. Results of the simulations for $10 [\frac{m^2}{kg}]$ space object during low solar activities with artificial reduction of the uncertainty

window achieved without the artificial reduction of the uncertainty for the same

simulations, i.e. 1.54039 [dd] (see table 4.3), it is possible to note a reduction R of:

$$R = \frac{1.54039 - 0.66513}{1.54039} = 56.82\%$$

Moreover, the initial circular orbits of the simulations show an oscillation of different amplitude in altitude during the decay phase, presenting a different level of ellipticity depending on the area to mass ratio and the level of solar activity, as it has been illustrated in chapter 4. Therefore, follow up work includes: 1) the use of a more accurate time series analysis tool (developing one if necessary) in order to achieve a tighter range of the predicted indices and consequently a tighter re-entry time window; 2) the further analysis of the before mentioned variation of the ellipticity during the orbit propagation from the initial circular orbit; 3) the exploration of the use of the same techniques and models presented in this Thesis to analyse the evolution during the decay phase of different kind of initial orbits at different altitudes.

Bibliography

- [1] J Geul, E Mooij, and R Noomen. “GOCE statistical re-entry predictions”. In: *Proceedings of 7th European Conference on Space Debris*. 2017.
- [2] Changyong He et al. “Review and comparison of empirical thermospheric mass density models”. In: *Progress in Aerospace Sciences* (2018).
- [3] Matthew Horsley. *Satellite re-entry modeling and uncertainty quantification*. Tech. rep. Lawrence Livermore National Lab.(LLNL), Livermore, CA (United States), 2012.
- [4] H Klinkrad. “On the use of atmosphere models in re-entry predictions”. In: *Environment Modeling for Space-Based Applications*. Vol. 392. 1996, p. 287.
- [5] H Klinkrad and E Doornbos. “Modeling of Space Weather Effects on Satellite Drag”. In: *35th COSPAR Scientific Assembly*. Vol. 35. 2004, p. 2000.
- [6] Qiaoli Kong et al. “Performance of Three Atmospheric Density Models on Precise Orbit Determination for Haiyang-2A Satellite Using DORIS Data”. In: *Civil Infrastructures Confronting Severe Weathers and Climate Changes Conference*. Springer. 2018, pp. 126–135.
- [7] S Lemmens et al. “Calibration of radar based re-entry predictions”. In: *Proceedings of the 5th International GOCE User Workshop. ESA Publications Division, European Space Agency, Noordwijk, The Netherlands*. 2014.
- [8] Edmondo Minisci et al. “Uncertainty treatment in the GOCE re-entry”. In: *1st IAA Conference on Space Situational Awareness (ICSSA)*. 2017.
- [9] Victor UJ Nwankwo, Sandip K Chakrabarti, and Robert S Weigel. “Effects of plasma drag on low Earth orbiting satellites due to solar forcing induced perturbations and heating”. In: *Advances in Space Research* 56.1 (2015), pp. 47–56.

- [10] Massimiliano Vasile. “Practical Uncertainty Quantification in Orbital Mechanics”. In: *Satellite Dynamics and Space Missions*. Springer, 2019, pp. 291–328.
- [11] Massimiliano L Vasile et al. “Analysis of the de-orbiting and re-entry of space objects with high area to mass ratio”. In: *AIAA/AAS Astrodynamics Specialist Conference*. 2016, p. 5678.
- [12] B Bastida Virgili et al. “GOCE re-entry campaign”. In: *5th international GOCE user workshop, Paris, France*. 2014.
- [13] B Bastida Virgili et al. “PRACTICALITIES OF RE-ENTRY PREDICTIONS—THE VEGA-01 AVUM CASE”. In: () .
- [14] Benjamin Bastida Virgili et al. “Combining observations for re-entry purposes”. In: (2018).
- [15] Vasily S Yurasov et al. “Reentry time prediction using atmospheric density corrections”. In: *Journal of guidance, control, and dynamics* 31.2 (2008), pp. 282–289.